1 ACE2-lentiviral transduction enables mouse SARS-CoV-2 infection and mapping of receptor interactions

2

3 Short title: Mouse SARS-CoV-2 infection using ACE2-lentivirus

4

5 Daniel J. Rawle[1*], Thuy T. Le[1], Troy Dumenil[1], Kexin Yan[1], Bing Tang[1], Cameron Bishop[1], Andreas

6 Suhrbier[1,2].

7

8 [1] Immunology Department, QIMR Berghofer Medical Research Institute, Brisbane, Queensland. 4029,

9 Australia.

10 [2] Australian Infectious Disease Research Centre, GVN Center of Excellence, Brisbane, Queensland 4029

11 and 4072, Australia.

12

13 [*]Corresponding author. Email: Daniel.Rawle@qimrberghofer.edu.au

14

15

16

17

18

19

20

21

22

23

24

25

26

**ABSTRACT**

SARS-CoV-2 uses the human ACE2 (hACE2) receptor for cell attachment and entry, with mouse ACE2 (mACE2) unable to support infection. Herein we describe an ACE2-lentivirus system and illustrate its utility for *in vitro* and *in vivo* SARS-CoV-2 infection models. Transduction of non-permissive cell lines with hACE2 imparted replication competence, and transduction with mACE2 containing N30D, N31K, F83Y and H353K substitutions, to match hACE2, rescued SARS-CoV-2 replication. Intranasal hACE2-lentivirus transduction of C57BL/6J mice permitted significant virus replication in lungs. RNA-Seq analyses illustrated that the model involves an acute inflammatory disease followed by resolution and tissue repair, with a transcriptomic profile similar to that seen in COVID-19 patients. Intranasal hACE2-lentivirus transduction of IFNAR$^{-/-}$ and IL-28RA$^{-/-}$ mice lungs was used to illustrate that loss of type I or III interferon responses have no significant effect on virus replication. However, their importance in driving inflammatory responses was illustrated by RNA-Seq analyses. We also demonstrate the utility of the hACE2-lentivirus transduction system for vaccine evaluation in C57BL/6J mice. The ACE2-lentivirus system thus has broad application in SARS-CoV-2 research, providing a tool for both mutagenesis studies and mouse model development.

**AUTHOR SUMMARY**

SARS-CoV-2 uses the human ACE2 (hACE2) receptor to infect cells, but cannot infect mice because the virus cannot bind mouse ACE2 (mACE2). We use an ACE2-lentivirus system *in vitro* to identify four key amino acids in mACE2 that explain why SARS-CoV-2 cannot infect mice. hACE2-lentivirus was used to express hACE2 in mouse lungs *in vivo*, with the inflammatory responses after SARS-CoV-2 infection similar to those seen in human COVID-19. Genetically modified mice were used to show that type I and III interferon signaling is required for the inflammatory responses. We also show that the hACE2-lentivirus mouse model can be used to test vaccines. Overall this paper demonstrates that our hACE2-lentivirus system has multiple applications in SARS-CoV-2 and COVID-19 research.

2

## INTRODUCTION

Severe acute respiratory syndrome coronavirus 2 (SARS-CoV-2) has spread rapidly into a global pandemic (1). SARS-CoV-2 infection can be asymptomatic, but is also the etiological agent of coronavirus disease 2019 (COVID-19), with acute respiratory distress syndrome (ARDS) representing a common severe disease manifestation (2). The SARS-CoV-2 pandemic has sparked unprecedented global research into understanding mechanisms of virus replication and disease pathogenesis, with the aim of generating new vaccines and treatments. Key to these efforts has been the development of animal models of SARS-CoV-2 infection and COVID-19 disease (3).

The receptor binding domain (RBD) of the spike glycoprotein of SARS-CoV-2 binds human Angiotensin-Converting Enzyme 2 (hACE2) as the primary receptor for cell attachment and entry (4). Mice do not support productive virus replication because the SARS-CoV-2 spike does not bind to mouse ACE2 (mACE2) (5). Expression of hACE2 in mice via a transgene allows SARS-CoV-2 infection and provides mouse models that recapitulate aspects of COVID-19. In such models hACE2 is expressed under control of various promoters, including K18 (6-12), mACE2 (13, 14), HFH4 (15), or chicken β-actin (16). These mouse models all differ in various aspects including level of virus replication, disease manifestations and tissue tropisms (3), but do not provide a simple mechanism whereby genetically modified (GM) or knock-out mice can be exploited for SARS-CoV-2/COVID-19 research. Two systems that do allow the latter, involve transient hACE2 expression in mouse lungs using adenovirus vectors (Ad5) or adeno-associated virus (AAV), which impart the capacity for productive SARS-CoV-2 replication in mouse lungs (10, 17, 18). A third model involves use of mouse adapted SARS-CoV-2 (19-21), although use of this mutated virus may complicate evaluation of interventions targeting human SARS-CoV-2.

Lentivirus-mediated gene expression in mice lung epithelium has been investigated as a treatment for cystic fibrosis and provides long term expression of the cystic fibrosis transmembrane conductance regulator (CFTR) (22-28). These studies demonstrated that VSV-G pseudotyped lentivirus can transduce mouse airway epithelial cells and their progenitors resulting in long-term gene expression. Herein we

3

79    describe an ACE2-lentiviral system that conveys SARS-CoV-2 replication competence *in vitro* and allows

80    productive infection of mouse lungs *in vivo*. We illustrate that GM mice can thereby be accessed for

81    SARS-CoV-2/COVID-19 research, with experiments using IFNAR$^{-/-}$ and IL-28RA$^{-/-}$ mice showing the

82    importance of type I and III IFN responses for SARS-CoV-2-induced inflammation. We also illustrate

83    the use of hACE2-lentiviral transduction of lungs of wild-type C57BL/6J mice for evaluation of vaccines.

84

85    **RESULTS**

86    **hACE2-lentiviruses for evaluating the role of RBD binding residues**

87    hACE2 coding sequence (optimized for mouse codon usage) was cloned into the dual promoter lentiviral

88    vector pCDH-EF1α-MCS-BGH-PGK-GFP-T2A-Puro (herein referred to as pCDH) (Figure 1A), which

89    had been modified to contain the full length EF1α promoter. Previous studies have shown that the EF1α

90    promoter effectively drives gene expression after intranasal VSV-G pseudotyped lentivirus transduction

91    of mouse lungs (29). The GFP marker and puromycin resistance gene (cleaved from GFP by T2A) are

92    expressed from a separate 3-phosphoglycerate kinase (PGK) promoter (Figure 1A). VSV-G pseudotyped

93    pCDH-hACE2 lentivirus was produced by co-transfection of the lentiviral vector with VSV-G and Gag-

94    Pol-Rev plasmids in HEK293T cells, and was used to transduce HEK293T (human embryonic kidney)

95    cells followed by puromycin selection. HEK293T cells do not express hACE2 (30) and therefore do not

96    support SARS-CoV-2 replication, whereas HEK293T cells transduced with hACE2 supported significant

97    virus replication (Figure 1B). A T92Q mutation in hACE2 was introduced to determine if removing the

98    N90 glycosylation motif increased SARS-CoV-2 replication, as computer-based modelling predicted

99    enhanced affinity for spike RBD with removal of this glycan (31, 32). We also introduced K31N/K353H

100    and T27Y/L79Y/N330Y mutations into hACE2 as these changes were predicted by computer modeling to

101    reduce and enhance affinity for spike RBD (31), respectively. HEK293T cells expressing these

102    aforementioned hACE2 mutations did not significantly affect SARS-CoV-2 replication (Figure 1B),

103    illustrating that *in silico* affinity predictions do not always translate to differences in virus replication.

104

105 **Characterizing residues responsible for the inability of mACE2 to support SARS-CoV-2 replication**

106 The ACE2-lentivirus system was used to introduce amino acid substitutions into mACE2 to identify the

107 amino acids that are responsible for restricting SARS-CoV-2 replication in mACE2-expressing cells.

108 Analysis of crystal structures and species susceptibilities has suggested residues that may be responsible

109 for the differences in binding of the RBD to hACE2 and mACE2 (33-37). Based on these *in silico*

110 studies, we identified seven residues potentially responsible for the human-mouse differences. mACE2-

111 lentivirus vectors were then generated that contained all seven substitutions

112 (N30D/N31K/T79L/S82M/F83Y/A329E/H353K), with two further vectors constructed to identify the

113 minimum requirements for SARS-CoV-2 replication. The latter contained a subset of the seven changes;

114 four amino acid changes (N30D/N31K/F83Y/H353K) and two amino acid changes (N31K/H353K).

115 As expected HEK293T cells expressing mACE2 did not support productive SARS-CoV-2

116 replication, and CPE was not observed. In contrast, all three mACE2 mutants significantly rescued virus

117 replication and infection resulted in CPE (Figure 1C-D). However, virus replication was significantly

118 lower for cells expressing mACE2 with only two substitution (N31K/H353K) (Figure 1C) and infection

119 produced less CPE (Figure 1D). Thus two amino acid changes (N31K and H353K) in mACE2 were

120 sufficient to support SARS-CoV-2 replication; however, at least four changes

121 (N30D/N31K/F83Y/H353K) were required for virus replication and CPE to be comparable to cells

122 expressing hACE2. These studies highlight the utility of the ACE2-lentivirus system for studying the role

123 of ACE2 residues in productive SARS-CoV-2 infections.

124

125 **Modeling the RBD:ACE2 key interactions for mouse, human and virus variants**

126 Of all the potential interactions between the RBD and ACE2 previously identify by X ray

127 crystallography and of all the amino acid differences between human and mouse ACE2 (33, 37), our data

128 identified a key role for 4 ACE2 mutations for conferring SARS-CoV-2 infectivity on mACE2 expressing

129 cells. Modeling of the interactions between these 4 mutations and the RBD predict improved interactions

130 between the virus and the receptor (Figure 1E), providing an explanation for the gain of function for the

131    mutated mACE2. The F83Y substitution replaced a non-polar interaction between mACE2-F83 and

132    RBD-N487, with a polar interaction between hACE2-Y83 and RBD-N487. The N31K substitution

133    created new interactions between ACE2-K31 and RBD-Q493. The N30D substitution created a salt

134    bridge interaction between ACE2-D30 and RBD-K417. Lastly, the H353K substitution created a new

135    hydrogen bond with RBD-G496.

136        Recently, SARS-CoV-2 variants have emerged with mutations in the RBD, with two of the key

137    mutations involving interactions with hACE2 residues 30 and 353 (38). Republic of South Africa (RSA)

138    variants (B.1.351 and 501Y.V2) have the RBD mutations K417N and N501Y, and the United Kingdom

139    (UK) variants (B.1.1.7 and 501Y.V1) have the N501Y mutation (38). Modelling predicts that the K417N

140    mutation would result in the gain of an interaction between RBD N417 and mACE2-Q34, whereas the

141    interaction between K417 and hACE2-D30 would be lost (Figure 1F). The selection for RBD-K417N in

142    humans may therefore be more related to antibody escape (39, 40), rather than improving interactions

143    with hACE2. The N501Y mutation in the RBD is predicted to generate new interactions between Y501

144    with mACE2-H353, and new polar interactions between Y501 and hACE2-K353 (Figure 1F). Our

145    modeling supports the observation that viruses with K417N and N501Y mutations have increased affinity

146    for mACE2, with both appearing in mouse-adapted SARS-CoV-2 (41).

147

148    **hACE2-lentivirus transduction of mouse cell lines imparts SARS-CoV-2 replication competence**

149    To determine whether hACE2-lentivirus transduction could make mouse cell lines SARS-CoV-2

150    replication competent and thus available for SARS-CoV-2 research, 3T3 (mouse embryonic fibroblasts)

151    and AE17 (mouse lung mesothelioma cell line) cells were transduced with hACE2. Significant virus

152    replication was seen in transduced cells (Supplementary Figure 1), although somewhat lower than that

153    seen in transduced HEK293T cells. Overt CPE was not seen (Supplementary Figure 1). This illustrates

154    that the hACE2-lentivirus system can be used for mouse cell lines, but that the efficiency of viral

155    replication may be cell line or cell type dependent.

156

6

157 **SARS-CoV-2 replication in hACE2-lentivirus transduced C57BL/6J, IFNAR$^{-/-}$ and IL-28RA$^{-/-}$ mice**

158 **lung**

159 To illustrate the utility of the hACE2-lentivirus system for use in GM mice, we investigated the role of

160 type I and type III IFN receptor signaling in SARS-CoV-2 infections. C57BL/6J, IFNAR$^{-/-}$ and IL-28RA$^{-}$

161 $^{/-}$ were inoculated intranasally (i.n.) with 1.2-2.2×10$^4$ transduction units of hACE2-lentivirus, equivalent to

162 approximately 190-350 ng of p24 per mice (Figure 2A). An hour prior to administration of lentivirus,

163 mice were treated i.n. with 1% lysophosphatidylcholine (LPC) to enhance transduction efficiency (25,

164 42). One week later mice were challenged with SARS-CoV-2 (10$^5$ CCID$_{50}$ i.n. per mice), and lungs were

165 collected at 2, 4 and 6 days post infection for C57BL/6J and IFNAR$^{-/-}$ mice and day 2 for IL-28RA$^{-/-}$

166 mice (Figure 2A). Mice did not display overt clinical symptoms or weight loss (Figure 2B), consistent

167 with some studies using Ad5-hACE2 (10), but not others (43). RT-qPCR analyses indicated similar levels

168 of hACE2 mRNA after transduction of mouse lungs in each of the 3 mouse strains, with expression

169 maintained over the 6 day course of the experiment at levels significantly higher than untransduced mice

170 (Figure 2C).

171 Lungs from infected C57BL/6J, IFNAR$^{-/-}$ and IL-28RA$^{-/-}$ were analyzed for infectious virus tissue

172 titers. Untransduced lungs showed no detectable virus titers (Figure 2D), whereas hACE2-lentivirus

173 transduced lungs showed significant viral titers ranging from 10$^2$ to 10$^5$ CCID$_{50}$/g for all strains of mice on

174 day 2, with titers dropping thereafter (Figure 2D). Viral RNA levels were measured using RT-qPCR, with

175 untransduced lungs showing low and progressively decaying levels post-inoculation (Figure 2E). For all

176 hACE2-lentivirus transduced lungs, significantly elevated and persistent viral RNA levels were seen for

177 all strains and at all time points by RT-qPCR (Figure 2E). Reducing viral titers and lingering viral RNA

178 have been reported previously for K18-hACE2 mice (9) and has also been suggested in human infections

179 (44). RNA-Seq also illustrated that virus replication in hACE2-lentivirus transduced lungs, K18-hACE2

180 transgenic mice and Ad5-hACE2 transduced lungs (43) were not significantly different when normalized

181 to hACE2 mRNA expression (Figure 2F), suggesting comparable hACE2 translation efficiencies and

182 SARS-CoV-2 replication efficiencies in these different expression systems.

7

183        Importantly, no significant differences in viral loads emerged between C57BL/6J, IFNAR$^{-/-}$ and

184    IL-28RA$^{-/-}$ mice (Figure 2D, E). This remained true even when viral RNA levels were normalized to

185    hACE2 mRNA levels (Supplementary Figure 2). Similar results were obtained by RNA-Seq, with viral

186    read counts not significantly different for the 3 mouse strains (Supplementary Figure 3A-D). Thus using

187    three different techniques, no significant effects on viral replication could be seen in mice with type I or

188    type III IFN receptor deficiencies.

189

190    **SARS-CoV-2 replication in hACE2-lentivirus transduced mice lung induces inflammatory**

191    **signatures by day 2 post-infection**

192    To determine the innate responses to SARS-CoV-2 replication in hACE2-transduced mouse lungs, gene

193    expression in lungs of infected hACE2-transduced mice was compared with infected untransduced mice

194    on day 2 post-infection using RNA-Seq. Differentially expressed genes (DEGs) between these groups

195    were identified using a false discovery rate (FDR, or q value) threshold of <0.05 (Figure 3A;

196    Supplementary Table 1A-C). Of the 110 DEGs, 95 were upregulated, with ≈40% of these classified as

197    type I IFN-stimulated genes (ISGs) as classified by Interferome (using conservative settings that only

198    included genes validated *in vivo* for mice) (Figure 3B, full list in Supplementary Table 1D). Type III

199    ISGs are known to be poorly annotated in this database, and so this analysis likely under-estimates the

200    number of such ISGs.

201        Ingenuity Pathway Analysis (IPA) of the 110 DEGs produced a series of pro-inflammatory

202    Upstream Regulators (USRs) (Supplementary Table 1E-F) and included Th1, Th2 and Th17-associated

203    cytokine USRs, as well as type I IFN USRs (Figure 3C). SARS-CoV-2-specific T cells in humans were

204    reported to be predominantly Th1-associated, but Th2-associated cytokines were also identified (45). A

205    cytokine and type I IFN DEG list has been published for a RNA-Seq analysis of SARS-CoV-2 infected

206    K18-hACE2 transgenic mice (9). These DEG lists were used to interrogate the full pre-ranked (fold

207    change) gene list (Figure 3A, Supplementary Table 1B) by Gene Set Enrichment Analysis (GSEA).

208    Significant enrichments were observed (Figure 3D), indicating similar cytokine and type I interferon

209  (IFN) responses after SARS-CoV-2 infection of K18-hACE2 transgenic and hACE2-lentivirus transduced

210  mice.

211      IPA *Diseases and Functions* analysis of the 110 DEGs revealed a series of annotations dominated

212  by cellular infiltration and innate responses signatures (Figure 3E, Supplementary Table 1G-H).  Several

213  of the annotations were associated with monocytes and macrophages (Figure 3E), consistent with a

214  previous report showing that inflammatory monocyte-macrophages were the major source of

215  inflammatory cytokines in mouse adapted SARS-CoV infected mice (46).  The cellular infiltrates in

216  COVID-19 patient lungs is also dominated by monocyte-macrophages with a suggested role in severe

217  disease (47).  Innate immune signaling was also the dominant signature in other analyses including GO

218  Biological Processes and Cytoscape (Supplementary Table 1I-J).

219      GSEA analysis using the >31,000 gene signatures available from the molecular signatures

220  database (MSigDB), indicated significant negative enrichment (negative NES scores) of gene sets

221  associated with translation and mitochondrial electron transport chain function (Supplementary Table

222  1K).  Translation inhibition by SARS-CoV-2 Nsp1 via the blocking of mRNA access to ribosomes has

223  been reported previously (48, 49).  SARS-CoV-2 down-regulation of genes associated with cellular

224  respiration and mitochondrial function has also been shown in human lung (50).

225      DEGs from human COVID-19 lung (51) were also enriched in our hACE2-lentivirus transduced

226  mouse lungs, and analysis of the core enriched genes indicated the similarity was due to cytokine, IFN,

227  chemokine and inflammatory signaling genes (Figure 3F, Supplementary Table 1L-M).  Another human

228  COVID-19 lung dataset was also interrogated (52) and the results again illustrated enrichment of immune-

229  related DEGs in the hACE2-lentivirus transduced mice (Supplementary Table 1N).

230      Overall these analyses illustrate that SARS-CoV-2 infection in hACE2-lentivirus transduced

231  C57BL/6J mice lungs significantly recapitulate responses seen in other murine models and in COVID-19

232  patients.

233

234

9

235 **Day 6 post-infection is characterized by inflammation resolution and tissue repair signatures**

236 To determine how response profiles progress in the hACE2-lentivirus model, RNA-Seq was used to

237 compare lungs on day 2 with lungs on day 6 post-infection, with day 6 broadly representing the time of

238 severe lung disease in the K18-hACE2 model (9). As noted above (Figure 2D), the virus titers had

239 dropped in hACE2-lentivirus transduced mice lung over this time period by ≈2.8 logs, and severe disease

240 (typically measured by weight loss) was not evident in this hACE2-lentivirus model (Figure 2B). In both

241 hACE2-lentivirus transduced and untransduced C57BL/6J mice there was a clear evolution of responses

242 from day 2 to day 6 post-infection; however, DEGs obtained from the former were largely distinct from

243 DEGs obtained from the latter (Figure 4A). The RNA-Seq data thus illustrated that the DEGs associated

244 with virus infection were distinct from those associated with virus inoculation (Figure 4A). RNA-Seq of

245 infected lungs provided 551 DEGs, 401 up-regulated and 150 down-regulated (Figure 4B, Supplementary

246 Table 2A-C).

247 IPA USR analyses of the 551 DEGs showed a clear reduction in inflammatory cytokine

248 annotations, although the IL4 signature remained a dominant feature on day 6 (Figure 4C, Supplementary

249 Table 2D-E). A Th2 skew and IL-4 have both been associated with lung damage in COVID-19 patients

250 (53). On day 6 there was an up-regulation of USRs primarily associated with tissue repair (Figure 4D,

251 Supplementary Table 2F); MAPK1 (also known as ERK) and MAPK9 (54), BMP7 (55), TCF7L2 (56),

252 and KLF4 (57, 58). B and T cell-associated USRs were also seen (Figure 4D, green circles) (59-61),

253 consistent with development of an adaptive immune response. A relatively minor PARP1 signature was

254 identified (Figure 4D), with PARP inhibitors being considered for COVID-19 therapy (62, 63). A strong

255 signature associated with estrogen receptor 1 (ESR1) was observed (Figure 4D), with estrogen having

256 anti-inflammatory properties and believed to be associated with reduced COVID-19 severity in women

257 (64-66), and reduced SARS-CoV disease severity in female mice (46, 67). Follicle stimulating hormone

258 (FSH) (Figure 4D) stimulates estrogen production, and inhibin subunit alpha (INHA) is involved in the

259 negative feedback of FSH production (68). IPA Diseases and Functions analysis, Cytoscape, and GO

260 Biological Processes analyses further supported the contention that on day 6 inflammation had abated and

10

261     tissue repair was underway (Supplementary Table 2G-L).

262         The >31,000 gene sets available in MSigDB were used to interrogate the complete gene list (pre-

263     ranked by fold change) for day 6 versus day 2 (Supplementary Table 2B) by GSEA.  A highly significant

264     negative enrichment for inflammatory response, and a highly significant positive enrichment for cilium

265     development was seen (Figure 4E).  Cilia in mammals are found in the lining of the respiratory

266     epithelium.  These GSEAs thus provide further support for the conclusion above, together arguing that in

267     the hACE2-lentivirus model, day 6 post infection is characterized by inflammation resolution and tissue

268     repair.

269

270     **Type I and III IFN signaling is required for SARS-CoV-2-induced lung inflammation**

271     To determine what responses to SARS-CoV-2 infection are dependent on type I IFN signaling, the

272     lentivirus system was used to analyze IFNAR$^{-/-}$ mice lung using RNA-Seq.  IFNAR$^{-/-}$ and C57BL/6J mice

273     were transduced with hACE2-lentivirus and were then infected with SARS-CoV-2 and lungs harvested

274     for RNA-Seq on days 2 and 6 post-infection.  The largest impact of type I IFN signaling deficiency was

275     seen on day 2 post infection (Figure 5A), consistent with disease resolution on day 6 (Figure 4C-E).  The

276     total number of DEGs for IFNAR$^{-/-}$ versus C57BL/6J mouse lungs on day 2 was 192, with most of these

277     down-regulated (Figure 5A, Supplementary Table 3A-C).  Viral reads were not significantly different

278     between these two mouse strains (Figure 5A), confirming that knocking out type I IFN signaling is

279     insufficient to significantly affect SARS-CoV-2 replication (69).

280         We showed in Figure 3 that RNA-Seq analysis revealed 110 DEGs associated with inflammatory

281     responses when hACE2-transduced versus untransduced C57BL/6J mouse lungs on day 2 post infection

282     were compared.  When the same comparison was made for hACE2-lentivirus transduced versus

283     untransduced lungs in SARS-CoV-2 infected IFNAR$^{-/-}$ mice, only 1 DEG (Kcnk5) was identified (Figure

284     5B).  This clearly illustrated that the inflammatory responses on day 2 in C57BL/6J mice (Figure 3C)

285     required intact type I IFN signaling.

286         As a control, the number of DEGs for IFNAR$^{-/-}$ mice versus C57BL/6J in untransduced lungs was

11

287    determined. Although virus replication (hACE2-lentivirus transduced lung) provided 192 DEGs, virus

288    inoculation (untransduced lung) provided only 16 DEGs (Figure 5C). Thus again, virus inoculation had a

289    limited effect on these analyses, with DEGs largely associated with virus infection.

290         Type III IFN is thought to act as a first-line of defense against infection at epithelial barriers, with

291    the more potent and inflammatory type I IFN response kept in reserved in the event the first line of

292    defense is breached (70, 71). As type III IFN signaling has been implicated in reducing SARS-CoV-2

293    infection *in vitro* (72), the aforementioned analyses on day 2 was repeated in IL-28RA$^{-/-}$ mice. Viral reads

294    were not significantly different between these two mouse strains (Figure 5D), confirming that knocking

295    out type III IFN signaling was insufficient to significantly affect SARS-CoV-2 replication (69, 73). The

296    DEG list for IL-28RA$^{-/-}$ versus C57BL/6J mice comprised 132 genes (Supplementary Table 4A-C), of

297    which 84 were down-regulated (Figure 5D). Perhaps surprisingly, the DEGs were mostly different from

298    that seen in IFNAR$^{-/-}$ mice (Figure 5D), arguing that the ISGs stimulated by type I and III IFNs are largely

299    distinct.

300         The majority (90%) of the 178 down-regulated DEGs in IFNAR$^{-/-}$ versus C57BL/6J mice on day

301    2 post infection were ISGs as defined by Interferome (using *in vivo* and mouse only settings) (Figure 5E,

302    top and Supplementary Table 3D). Of the 84 down-regulated genes in IL-28RA$^{-/-}$ lungs, only 27% were

303    identified as ISGs (Figure 5E, bottom and Supplementary Table 4D). However, there are no annotations

304    in the Interferome database for type III ISGs in mice, and changing the settings to include human data

305    (which is also under-annotated for type III IFN) did not increase the number of type III ISGs in our search

306    using down DEGs from IL-28RA$^{-/-}$ lungs.

307         To determine the pathways regulated by type I and III IFN in response to SARS-CoV-2 infection,

308    IPA USR analyses was performed on DEG lists from day 2 for hACE2-lentivirus transduced lungs for

309    IFNAR$^{-/-}$ versus C57BL/6J (192 DEGs) and IL-28RA$^{-/-}$ versus C57BL/6J (132 DEGs). IPA USR

310    signatures associated with pro-inflammatory cytokine signaling were significantly reduced in both

311    IFNAR$^{-/-}$ and, to a lesser extent, IL-28RA$^{-/-}$ mice when compared to C57BL/6J mice (Figure 5F, full lists

312    in Supplementary Table 3E and 4E). The USR annotations for type I and III IFN receptor deficiencies

313 were largely similar (Figure 5F), although they arose from a largely distinct set of DEGs (Figure 5D).

314 This likely reflects expression of type I and type III IFN by different cell types with differing response

315 profiles to the same cytokines (70).

316  Taken together these results illustrate that while there was no significant effects on viral

317 replication, lungs from type I and type III IFN receptor knockout mice both had a significantly blunted

318 acute pro-inflammatory response following SARS-CoV-2 infection.  The importance of type I IFN for

319 inflammation was reported previously using the AAV-hACE2 system (18).

320

321 **Immunization with infectious or UV-inactivated SARS-CoV-2 protects against virus infection**

322 To evaluate the utility of the hACE2-lentivirus mouse model of SARS-CoV-2 replication for vaccine

323 studies, C57BL/6J mice were immunized twice subcutaneously (s.c.) with either infectious SARS-CoV-2

324 or UV-inactivated SARS-CoV-2 (74) formulated with adjuvant (Figure 6A).  Serum SARS-CoV-2

325 neutralization titers were determined post-boost, and revealed all mice had significant serum

326 neutralization titers (Figure 6B), comparable with the higher end levels seen in people with past SARS-

327 CoV-2 infections (75).  On day 2 post challenge all mice were sacrificed.  All mouse lungs had detectable

328 hACE2 mRNA by RT-qPCR, with levels higher in unvaccinated mice (Figure 6C), likely due to immune

329 cell infiltrates (see below) diluting hACE2 mRNA.  Mice immunized with either infectious or UV-

330 inactivated SARS-CoV-2 showed significant reductions in viral RNA levels by RT-qPCR (Figure 6D) in

331 tissue titrations (Figure 6E) and by RNA-Seq read counts (Figure 6F).  These immunizations thus

332 protected mice against significant viral infections and demonstrated the utility of hACE2-lentivirus

333 transduced mice as a model for vaccine evaluation.

334  Lungs harvested on day 2 were also analyzed by RNA-Seq (Supplementary Table 5A-B), with

335 1376 DEGs identified for infectious virus immunization versus unimmunized (DEGs in Supplementary

336 Table 5C).  The DEGs were analyzed by IPA canonical pathways, USR analysis, and the Diseases and

337 Functions feature, which all showed infiltration signatures, dominated by T cell annotations

338 (Supplementary Table 5D-F).  This was confirmed by GSEA of human blood transcription modules (76)

13

339   against the pre-ranked (by fold change) gene list for immunized versus unvaccinated mice

340   (Supplementary Table 5G). This showed the expected enrichment of T cell and B annotations in

341   immunized mice (Figure 6F), and illustrated that protection against virus replication in lungs of

342   immunized mice was associated with a significant infiltration of lymphocytes. This aligns with studies

343   that suggest COVID-19 patients that induce an early SARS-CoV-2-specific T cell response have rapid

344   viral clearance and mild disease (77).

345

346   **DISCUSSION**

347   Herein we describe a hACE2-lentivirus transduction system that allows the use of C57BL/6J and GM

348   mice for SARS-CoV-2/COVID-19 research. Virus titer in hACE2-lentivirus transduced mice lung were

349   comparable to other studies using mice transduced with Ad5 or AAV expressing hACE2 (10, 17, 18).

350   These transduction methodologies avoid the fulminant brain infection seen in K18-hACE2 mice, with

351   infection of this organ the major contributor to mortality in the K18-hACE2 model (78, 79). The key

352   advantage of lentiviral over adenoviral systems is the integration of the lentiviral payload into the host cell

353   genome, thereby providing long-term stable expression. The hACE2-lentivirus thus provides a new

354   option for studying SARS-CoV-2 infection that can be readily applied using standard lentivirus

355   technology. We characterize the lentivirus-hACE2 model of SARS-CoV-2 infection in C57BL/6J mice,

356   and illustrate the use of lentivirus-hACE2 to assess the role of type I and type III IFNs in virus control and

357   inflammatory responses using IFNAR$^{-/-}$ and IL-28RA$^{-/-}$ mice, respectively. We also illustrate the use of

358   C57BL/6J mice transduced with lentivirus-hACE2 for SARS-CoV-2 vaccine evaluation.

359          The lentivirus-hACE2 C57BL/6J mouse model of SARS-CoV-2 infection shares many cytokine

360   signatures with those seen in human COVID-19 patients; IL-2, IL-10, IL-6, TNFα, IL-4, IL-1β, IFNγ and

361   CSF3 signatures were found in SARS-CoV2-infected lentivirus-hACE2 transduced C57BL/6J mice on

362   day 2 post infection, and elevated levels of these cytokines are found in COVID-19 patients (80, 81).

363   Several of these cytokines have been implicated as mediators of COVID-19; for instance, IL-6 (82-84),

364   IL-4 (53), IL-10 (85) and IFNγ (86). On day 6 post infection the lentivirus-hACE2 C57BL/6J mouse

14

365 model showed a series of signatures associated with tissue repair. Thus our RNA-Seq analyses illustrated

366 that this model involves an acute inflammatory disease followed by resolution and tissue repair.

367  hACE2-lentivirus transduction in IFNAR$^{-/-}$ and IL-28RA$^{-/-}$ mice was used to confirm that type I

368 IFN signaling (18) and show that type III IFN signaling are involved in driving inflammatory responses.

369 Virus replication was not significantly affected in IFNAR$^{-/-}$ and IL-28RA$^{-/-}$ mice, largely consistent with

370 other studies using different model systems, which indicate that knocking out both pathways (STAT1$^{-/-}$,

371 STAT2$^{-/-}$, or combined IFNAR$^{-/-}$/IL-28RA$^{-/-}$) is required before an impact on virus replication is seen (18,

372 69, 73, 87). A high level of cross-compensation is thus implicated, as is described in influenza infection

373 (71). *In vitro* experiments show that SARS-CoV-2 replication is sensitive to type I and III IFNs, although

374 infection does not stimulate particularly high levels of IFN (72, 88, 89). A number of SARS-CoV-2

375 encoded proteins inhibit IFN production and signaling (83, 90, 91). In infected cells, such inhibition of

376 signaling would limit the antiviral activity of IFNs, as well as limiting the positive feedback amplification

377 that is needed for high level IFN production (92). IFN therapies have been proposed for COVID-19

378 patients (93) and such treatment may induce an antiviral state in uninfected cells, thereby perhaps limiting

379 viral spread if given prophylactically or early during the course of infection (94). However, caution might

380 be warranted for such therapy during later stage COVID-19 as type I and III IFN signaling are shown

381 herein to drive inflammatory responses during SARS-CoV-2 infection, and are also known to have pro-

382 inflammatory activities in other settings (92).

383  Herein we also illustrate the use of the hACE2-lentivirus system to study the role of ACE2

384 residues on SARS-CoV-2 replication *in vitro*. Only four "mouse-to-human" changes in mACE2 (N30D,

385 F83Y, N31K, H353K) enabled full SARS-CoV-2 replication to levels similar to those seen for infection

386 of hACE2-expressing cells. These results suggest a CRISPR mouse with these substitutions would be

387 able to support SARS-CoV-2 infection and provide a model of COVID-19. Remarkably, a minimum of

388 only two substitutions in mACE2 (N31K, H353K) were sufficient for partial restoration of SARS-CoV-2

389 infection. Changing the same resides in hACE2 to their mouse equivalents (K31N, K353H) did not affect

390 virus replication compared to WT hACE2. Thus N31K and H353K allows binding of SARS-CoV2 to

15

391    mACE2, but K31N and K353H does not impair binding to hACE2.  Both K31N and K353H substitutions

392    were shown to be deleterious for SARS-CoV2 binding by *in silico* analyses.  However, the same analyses

393    implicated >25 other residues in hACE2 binding (31), with many of these potentially able to compensate

394    for the loss of native residues at K31 and K353.

395        In conclusion, we describe the development of a mouse model using intranasal hACE2-lentivirus

396    transduction to sensitize mice lung to SARS-CoV-2 infection, which recapitulated cytokine signatures

397    seen in other mouse models and COVID-19.  We demonstrate broad applicability of this new mouse

398    model in vaccine evaluation, GM mice infection, and *in vitro* evaluation of ACE2 mutants.

408

409    **AUTHOR CONTRIBUTIONS**

410    Conceptualization, D.J.R.; Methodology, D.J.R. and A.S.; Formal analysis, D.J.R., A.S., and T.D.;

411    Investigation, D.J.R., T.T.L., K.Y., B.T.; Data curation, D.J.R., A.S., and T.D.; Writing – original draft,

412    D.J.R.; Writing – review and editing, A.S. and D.J.R.; Visualization, D.J.R., A.S., T.D., and C.B;

413    Supervision, D.J.R. and A.S., Project administration, D.J.R. and A.S.; Funding acquisition, A.S. and

414    D.J.R.

415

416    **DECLARATION OF INTERESTS**

417    The authors declare no competing interests.

418

419    **DATA AVAILABILITY**

420    All raw sequencing data (fastq files) are available from the Sequence Read Archive (SRA), BioProject

421    accession: PRJNA701678.  All other data is available within the paper and supporting information files.

422

423    **FIGURE LEGENDS**

424    **Figure 1.  Mutational analyses of human and mouse ACE2 using ACE2-lentiviruses *in vitro*.  A)**

425    Schematic of pCDH-EF1α-ACE2-BGH-PGK-GFP-T2A-Puro lentiviral vector.  **B-C)** Growth kinetics of

426    SARS-CoV-2 over a three day time course in HEK293T cells transduced with WT or mutant hACE2 **(B)**

427    or mACE2 **(C)** infected at MOI=0.1.  Data is the mean of 1 (hACE2-T27Y/L79Y/N330Y and mACE2-

428    N31K/H353K) or 2 (all others) independent experiments with 2-3 replicates in each and error bars

429    represent SEM.  Statistics was determined using Repeated Measures Two-Way ANOVA comparing

430    untransduced (for B) or WT mACE2 (for C) with all others, and comparing mACE2-

431    N30D/N31K/F83Y/H353K with mACE2-N31K/H353K.  **D)** Inverted light microscopy images of

432    HEK293T cells transduced with the indicated ACE2 lentivirus and infected with SARS-CoV-2 at

433    MOI=0.1.  Images were taken at day 3 post infection and were representative of triplicate wells.  **E)**

434    Crystal structure of the spike RBD:hACE2 complex (PBD: 6M0J) (95) viewed in PyMOL and zoomed in

435    on key interactions between ACE2 residues identified in 'C-D' (hACE2 = blue, mACE2 = brown) and

436    spike RBD residues (orange).  Yellow dotted lines represent any contacts between chains within 3.5Å,

437    and blue dotted lines represent polar contacts.  Direction of black arrows indicate predicted enhanced

438    interactions.  **F)**  K417N and N501Y mutations (magenta) were introduced in the spike RBD to mimic the

439    Republic of South Africa (B.1.351 and 501Y.V2) and United Kingdom (B.1.1.7 and 501Y.V1) SARS-

440    CoV-2 variants.

441

442 **Figure 2. SARS-CoV-2 replication in hACE2-lentivirus transduced C57BL/6J, IFNAR^{-/-} and IL-**

443 **28RA^{-/-} mice lung. A)** Timeline of lentivirus transduction of mice lung and SARS-CoV-2 infection. **B)**

444 Percent weight loss for mice in C-E. Data represents the mean percent weight loss from day 0 and error

445 bars represent SEM. **C)** RT-qPCR of mice lung RNA using primers for hACE2 (introduced by lentivirus

446 transduction) normalized to mRPL13a levels. Data is for individual mice and is expressed as RNA copy

447 number calculated against a standard curve for each gene. Horizontal line indicates cut-off for reliable

448 detection, with all untransduced mice falling below this line. Statistics are by Kolmogorov Smirnov test

449 compared to untransduced samples. **D)** Titer of SARS-CoV-2 in mice lung determined using $CCID_{50}$

450 assay of lung homogenate. Horizontal line indicates the limit of detection of 1.57 $\log_{10}$ $CCID_{50}$/g.

451 Statistics are by Kolmogorov Smirnov test compared to untransduced mice. IFNAR^{-/-} versus

452 untransduced mice at day 2 post infection reaches significance by Kruskal-Wallis test (p=0.018). **E)** RT-

453 qPCR of mice lung RNA using primers for SARS-CoV-2 E gene normalized to mRPL13a levels. Data is

454 individual mice and is expressed as RNA copy number calculated using a standard curve. Statistics are by

455 Kolmogorov Smirnov test compared to untransduced mice. C57BL/6J hACE2-transduced versus

456 untransduced mice at day 4 post infection reaches significance by Kruskal-Wallis test (p=0.046). See

457 Supplementary Figure 2 for SARS-CoV-2 RNA copies normalised to hACE2 copies. **F)** SARS-CoV-2

458 read counts (also see Supplementary Figure 3) normalized to hACE2 read counts from RNA-seq data for

459 lentivirus-hACE2 transduced mice at day 2, K18-hACE2 transgenic mice at day 4, and Ad5-hACE2

460 transduced mice at day 2 (43). Not significant by Kolmogorov Smirnov or Kruskal-Wallis tests.

461

462 **Figure 3. SARS-CoV-2 replication in hACE2-lentivirus transduced mice lung induces**

463 **inflammatory signatures by day 2 post-infection. A)** Volcano plot of gene expression from RNA-seq

464 analyses of lung at day 2 comparing mice with and without hACE2-lentivirus transduction. Genes were

465 considered DEGs if they had a FDR value < 0.05 (above horizontal dotted line) (see Supplementary Table

466 1B-C for full gene and DEG lists). **B)** Interferome analysis of 95 up DEGs from 'A'. 38 of 95 up DEGs

467 (40%) were ISGs. Red = type I IFN, blue = type II IFN, green = type III IFN (see Supplementary Table

18

468 1D for full Interferome ISG list). **C)** Cytokine signatures identified by IPA USR analysis (see

469 Supplementary Table 1E-F for full and cytokine only USR lists) of 110 DEGs identified in 'A'. Circle

470 area reflects the number of DEGs associated with each USR annotation. USRs were grouped into three

471 categories; red = Th1 associated, green = Th2 associated, blue = Th17 associated, and black =

472 pleiotropic/other. The vertical dotted line indicates activation z-score of 0. **D)** GSEAs for cytokine-

473 related DEGs or type I IFN-related DEGs from Winkler et al. supplemental data (9) against the pre-ranked

474 all gene list (Supplementary Table 1B). Normalised enrichment score (NES) and nominal p-value are

475 shown. **E)** IPA diseases and functions analysis (see Supplementary Table 1G-H for full lists) of 110

476 DEGs identified in 'A'. The 23 annotations with the most significant p-value and with an activation z-

477 score of >2 were plotted with dots/lines indicating activation z-score and bars indicating $-\log_{10}$ p-value.

478 Annotations were grouped into two categories; cellular infiltration (blue) and innate responses (red). **F)**

479 GSEA for DEGs from human COVID-19 lung versus healthy control from Blanco-Melo et al. (51)

480 against the pre-ranked (by fold change) all gene list (Supplementary Table 1B). Normalised enrichment

481 score (NES) and nominal p-value are shown. Core enriched genes (see Supplementary Table 1L for full

482 core enriched gene list) determined by GSEA were entered into Enrichr and the top 10 GO Biological

483 Processes annotations sorted by p-value are shown (see Supplementary Table 1M for full GO processes

484 list).

485

486 **Figure 4. Day 6 post-infection is characterized by inflammation resolution and tissue repair**

487 **signatures. A)** Venn diagram for DEGs comparing day 6 versus 2 post infection with (red) and without

488 (green) hACE2-lentivirus transduction. Number of DEGs that are FDR<0.05 are shown. Mean virus titer

489 ($\log_{10}$ CCID$_{50}$/g) in lung tissue ± SEM (represents data shown in Figure 2D) is shown for hACE2

490 transduced mice at day 2 or 6 post infection. **B)** Volcano plot of gene expression from RNA-seq analyses

491 of hACE2-lentivirus transduced lung RNA comparing day 6 with day 2 (see Supplementary Table 2B-C

492 for gene and DEG lists). Genes were considered DEGs if they had a FDR value < 0.05 (above horizontal

493 dotted line). **C)** Cytokine signatures identified by IPA USR analysis (see Supplementary Table 2D-E for

494    full and cytokine only lists) of 551 DEGs identified in 'B' (Supplementary Table 2C).  Circle area reflects

495    the number of DEGs associated with each USR annotation.  USRs were grouped into four categories; red

496    = Th1 associated, green = Th2 associated, blue = Th17 associated, and black = pleiotropic/other.  The

497    vertical dotted line indicates activation z-score of 0.  **D)**  Upregulated USR signatures identified using IPA

498    analysis (see Supplementary Table 2F) of 551 DEGs identified in 'B'.  Circle area reflects the number of

499    DEGs associated with each USR annotation. USRs (excluding chemicals) with an activation z-score of >2

500    are shown and were grouped into five categories; green = B cell function, blue = tissue repair – endocrine

501    signaling, orange = tissue repair – growth factor, red = tissue repair – kinase, purple = tissue repair – Wnt

502    signaling.  **E)**  Selected plots from GSEA of entire MSigDB database using pre-ranked (by fold change)

503    'all' gene list (Supplementary Table 2B).  NES score and p-value is shown for the

504    "GO_inflammatory_response" and

505    "Wp_Genes_Related_To_Primary_Cilium_Development_Based_On_Crispr" annotations.

506

507    **Figure 5.  Type I and III IFN signaling is required for SARS-CoV-2-induced lung inflammation.  A)**

508    Venn diagram for number of DEGs (FDR<0.05) between IFNAR$^{-/-}$ versus C57BL/6J mice at day 2 or day

509    6 (green).  Mean $\log_{10}$ SARS-CoV-2 read count in RNA-seq data ± SEM is shown (red text = day 2, green

510    text = day 6). **B)** Venn diagram for number of DEGs (FDR<0.05) between plus versus minus hACE2-

511    lentivirus transduction comparing C57BL/6J (red) and IFNAR$^{-/-}$ (green) mice at day 2.  **C)** Venn diagram

512    for IFNAR$^{-/-}$ versus C57BL/6J mice at day 2 comparing hACE2-lentivirus transduced (red) or

513    untransduced (green) mice.  **D)** Venn diagram comparing IFNAR$^{-/-}$ versus C57BL/6J (red) and IL-28RA$^{-/-}$

514    versus C57BL/6J (blue) (see Supplementary Table 3B-C and 4B-C for full gene and DEG lists) mice at

515    day 2 (all mice had received hACE2-lentivirus transduction).  Mean $\log_{10}$ SARS-CoV-2 read count in

516    RNA-seq data ± SEM is shown (red text = IFNAR$^{-/-}$, black text = C57BL/6J, blue text = IL-28RA$^{-/-}$).  **E)**

517    Interferome analysis of down DEGs from 'D'.  See supplementary Table 3D and 4D for full Interferome

518    ISG list.  **F)** Signatures identified using IPA USR analysis of DEGs identified in 'D' for IFNAR$^{-/-}$ versus

519    C57BL/6J (red) and IL-28RA$^{-/-}$ versus C57BL/6J (blue).  Circle area reflects the number of DEGs

20

520    associated with each USR annotation.  Signatures were selected focusing on data previously identified in

521    'Figure 3C' (entire list is in Supplementary Table 3E and 4E).

522

523    **Figure 6.  Immunization with infectious or UV-inactivated SARS-CoV-2 protects against virus**

524    **infection.  A)** Timeline of mice immunization, lentivirus transduction and SARS-CoV-2 infection.  **B)**

525    Reciprocal 50% neutralization titers of naïve mice and infectious or UV SARS-CoV-2 immunized mice.

526    Horizontal dotted line represents the limit of detection (1 in 10).  Statistics are by Kolmogorov Smirnov

527    test.  **C)**  RT-qPCR of mice lung RNA using primers for hACE2 introduced by lentivirus transduction

528    normalized to mRPL13a levels. Data is individual mice and is expressed as RNA copy number calculated

529    against a standard curve for each gene.  Horizontal line indicates cut-off for reliable detection, with all

530    hACE2-negative mice falling below this line.  Statistics are by Kolmogorov Smirnov test.  **D)**  RT-qPCR

531    of mice lung RNA using primers for SARS-CoV-2 E gene normalized to mRPL13a levels. Data is

532    individual mice and is expressed as RNA copy number calculated against a standard curve for each gene.

533    Statistics are by Kolmogorov Smirnov test.  Unvaccinated versus UV-inactive CoV-2 vaccinated reaches

534    significance by Kruskal-Wallis test (p=0.034).  **E)**  Titer of SARS-CoV-2 in mice lung determined using

535    $CCID_{50}$ assay of lung homogenate.  Horizontal line indicates the limit of detection of 1.57 $\log_{10} CCID_{50}/g$.

536    Statistics are by Kolmogorov Smirnov test.  Unvaccinated versus UV-inactive CoV-2 vaccinated reaches

537    significance by Kruskal-Wallis test (p=0.028).  **F)**  Mean $\log_{10}$ SARS-CoV-2 read count at day 2 post-

538    infection in RNA-seq data ± SEM is shown (blue text = unvaccinated mice, red text = infectious SARS-

539    CoV-2 immunized mice).  GSEA for Blood Transcription Modules (BTMs) from Li et al. (76) against the

540    pre-ranked all gene list comparing unvaccinated versus infectious SARS-CoV-2 immunized (s.c) mice

541    lung at day 2 (all mice had hACE2-lentivirus transduction).  Selected BTM modules with a positive NES

542    score and p < 0.05 are shown (full list in Supplementary Table 5).  See Supplementary Table 5 for full

543    gene and DEG lists and full downstream analyses lists.

544

545

546 **MATERIALS and METHODS**

547 **Ethics statement**

548 All mouse work was conducted in accordance with the "Australian code for the care and use of animals

549 for scientific purposes" as defined by the National Health and Medical Research Council of Australia.

550 Mouse work was approved by the QIMR Berghofer Medical Research Institute animal ethics committee

551 (P3600, A2003-607). For intranasal inoculations, mice were anesthetized using isoflurane. Mice were

552 euthanized using $CO_2$ or cervical dislocation.

553

554 **Cell lines and SARS-CoV-2 culture**

555 Vero E6 (C1008, ECACC, Wiltshire, England; Sigma Aldridge, St. Louis, MO, USA), HEK293T (a gift

556 from Michel Rist, QIMR Berghofer), Lenti-X 293T (Takara Bio), AE17 (a gift from Delia Nelson,

557 Faculty of Health Sciences, Curtin Medical School), and NIH-3T3 (American Type Culture Collection,

558 ATCC, CRL-1658) cells were cultured in medium comprising DMEM for Lenti-X 293T cells or

559 RPMI1640 for all others (Gibco) supplemented with 10% fetal calf serum (FCS), penicillin

560 (100□IU/ml)/streptomycin (100□μg/ml) (Gibco/Life Technologies) and L-glutamine (2 mM) (Life

561 Technologies). Cells were cultured at 37°C and 5% $CO_2$. Cells were routinely checked for mycoplasma

562 (MycoAlert Mycoplasma Detection Kit MycoAlert, Lonza) and FCS was assayed for endotoxin

563 contamination before purchase (96). The SARS-CoV-2 isolate was kindly provided by Queensland

564 Health Forensic & Scientific Services, Queensland Department of Health, Brisbane, Australia. The virus

565 (hCoV-19/Australia/QLD02/2020) was isolated from a patient and sequence deposited at GISAID

566 (https://www.gisaid.org/; after registration and login, sequence can be downloaded from

567 https://www.epicov.org/epi3/frontend#1707af). Virus stock was generated by infection of Vero E6 cells

568 at multiplicity of infection (MOI)≈0.01, with supernatant collected after 2-3 days, cell debris removed by

569 centrifugation at 3000 x g for 15 min at 4°C, and virus aliquoted and stored at -80°C. Virus titers were

570 determined using standard $CCID_{50}$ assays (see below). The virus was determined to be mycoplasma free

571 using co-culture with a non-permissive cell line (i.e. HeLa) and Hoechst staining as described (97).

572

573 **CCID$_{50}$ assays**

574 Vero E6 cells were plated into 96 well flat bottom plates at $2x10^4$ cells per well in 100 µl of medium. For

575 tissue titer, tissue was homogenized in tubes each containing 4 ceramic beads twice at 6000 x g for 15

576 seconds, followed by centrifugation twice at 21000 x g for 5 min before 5 fold serial dilutions in 100 µl

577 RPMI1640 supplemented with 2% FCS. For cell culture supernatant, 10 fold serial dilutions were

578 performed in 100 µl RPMI1640 supplemented with 2% FCS. 100 µl of serially diluted samples were

579 added to Vero E6 cells and the plates cultured for 5 days at 37°C and 5% $CO_2$. The virus titer was

580 determined by the method of Spearman and Karber (a convenient Excel CCID$_{50}$ calculator is available at

581 https://www.klinikum.uni-heidelberg.de/zentrum-fuer-infektiologie/molecular-

582 virology/welcome/downloads).

583

584 **Lentivirus cloning**

585 ACE2 genes were cloned into pCDH-EF1α-MCS-BGH-PGK-GFP-T2A-Puro Cloning and Expression

586 Lentivector (System Biosciences, catalogue number CD550A-1), where the EF1α promoter was replaced

587 with the full length EF1α using NheI and ClaI restriction enzymes (New England Biolabs). Human ACE2

588 coding sequence (codon optimized for mouse) was cloned into the pCDH lentivector with PCR fragments

589 amplified using Q5® High-Fidelity 2X Master Mix (New England Biolabs) and the following primers;

590 vector backbone (pCDH amplified with Forward 5'- TAAATCGGATCCGCGG -3' and Reverse 5'-

591 AATTCGAATTCGCTAGC) and hACE2 insert (Forward 5'-

592 GCTAGCGAATTCGAATTATGAGCAGCAGCTCTTGGC -3' and Reverse 5'-

593 CCGCGGATCGCATTTATCAGAAGCTTGTCTGCACGT -3'). The pCDH fragment was digested with

594 DpnI (New England Biolabs) and was purified using QIAquick Gel Extraction Kit (QIAGEN), as was the

595 hACE2 fragment. Fragments were recombined using NEBuilder HiFi DNA Assembly Cloning Kit as per

596 manufacturer instructions. This was transformed into NEB® 10-beta Competent E. coli (High Efficiency)

597 (New England Biolabs) as per manufacturer instructions and plated on ampicillin agar plates overnight.

598    Colony PCR was performed using Q5 High-Fidelity 2X Master Mix (New England Biolabs) and the

599    hACE2 insert primers to identify a positive colony, which was grown in LB broth with ampicillin and

600    plasmid was purified using NucleoBond Xtra Midi kit (Machery Nagel).

601    All ACE2 mutant coding sequences were ordered from Twist Bioscience/Decode Science containing

602    EcoRI upstream and BamHI downstream.  Fragments were amplified using the using Q5® High-Fidelity

603    2X Master Mix (New England Biolabs) and the following primers; Forward 5'-

604    CCTGACCTTAGCGAATTCATG -3' and Reverse 5'- ACCTAGCCTCGCGGATC -3'.  PCR fragments

605    were purified using Monarch DNA Gel Extraction Kit (New England Biolabs), and were digested with

606    EcoRI and BamHI (New England Biolabs), as was the pCDH vector before purification again with

607    Monarch® DNA Gel Extraction Kit (New England Biolabs).  The ACE2 fragment was ligated with

608    pCDH vector using T4 DNA Ligase (New England Biolabs) as per manufacturer instructions and then

609    transformed into NEB® 10-beta Competent E. coli (High Efficiency) (New England Biolabs) as per

610    manufacturer instructions and plated on ampicillin agar plates overnight.  Colonies were grown in LB

611    broth with ampicillin and plasmid was purified using NucleoBond Xtra Midi kit (Machery Nagel).

612    Plasmids were confirmed by PCR with the cloning primers above and fragments were gel purified and

613    confirmed by Sanger sequencing with the forward primer.

614

615    **Lentivirus production, titration and cell line transduction**

616    ACE2 lentivirus was produced by co-transfection of HEK293T or Lenti-X HEK293T cells with the

617    pCDH-ACE2 plasmid, VSV-G and Gag-Pol using Lipofectamine 2000 Reagent (Thermo Fisher

618    Scientific) or Xfect Transfection Reagent (Takara Bio) as per manufacturer instructions.  Supernatant was

619    collected 2 days after transfection and centrifuged at 500 x g for 10 min, and this was concentrated using

620    Amicon Ultra-15 Centrifugal Filter Units with 100 kDa cutoff (Merck Millipore) as per manufacturer

621    instructions.  Lentivirus was titrated by serial dilution of lentivirus and incubating with 5000 HEK293T

622    cells in 96 well plates with 8 µg/ml polybrene for 3 days followed by GFP detection by flow cytometry

623    (BD Biosciences LSRFortessa).  Transduction units (TU) per ml was calculated by percentage of 5000

24

624    cells that are GFP positive multiplied by the dilution. For example if 2 µl lentivirus gives 5% GFP

625    positive cells, the TU/ml is ((5/100)*5000) * (1000/2) = 125,000 TU/ml.  The p24 equivalent (ng/ml) was

626    measured using Lenti-X GoStix Plus (Takara Bio) as per manufacturer instructions.

627    Cell lines were transduced by incubating with lentivirus and 8 µg/ml polybrene for 2-3 days followed by 5

628    µg/ml puromycin treatment until most resistant cells expressed GFP.  Cells were then infected with

629    SARS-CoV-2 at MOI 0.1 for 1 hr at 37°C, cells were washed with PBS and media replaced.  Culture

630    supernatant was harvested at the indicated timepoints and titered by $CCID_{50}$ assay as described.

631

632    **SARS-CoV-2 spike RBD:ACE2 mutagenesis modeling**

633    PyMOL v4.60 (Schrodinger) was used for mutagenesis of the crystal structure of SARS-CoV-2 spike

634    receptor-binding domain bound with ACE2 from the protein data bank (6M0J) (95).  The side chain

635    orientation (rotamer) with highest frequency of occurrence in proteins was chosen for all mutations.  Polar

636    interactions (blue lines) or any interactions within 3.5Å (yellow lines) were shown for selected residues.

637    The K417N and N501Y mutations in the UK variant (B.1.1.7) and RSA variant (B.1.351) were introduced

638    (38).

639

640    **UV-inactivated SARS-CoV-2 vaccine preparation and mice immunization**

641    120 ml of SARS-CoV-2 was inactivated with at least 7650 $J/m^2$ UVC in a UVC 500 Ultraviolet

642    Crosslinker (Hoefer).  Virus was determined to be inactivated by incubation with Vero E6 cells for 4 days

643    without development of CPE.  UV-inactive SARS-CoV-2 was then partially-purified using a 20% sucrose

644    cushion centrifuged at 175,000 x g for 3-4 hr using SW32Ti rotor (Beckman Coulter).  The sample that

645    has passed through the sucrose was collected and concentrated using Amicon Ultra-15 Centrifugal Filter

646    Units with 100 kDa cutoff (Merck Millipore).  For infectious SARS-CoV-2 immunization, virus was also

647    concentrated using Amicon Ultra-15 Centrifugal Filter Units with 100 kDa cutoff (Merck Millipore).

648    Mice were injected s.c. in the base of the tail with 100 µl of UV-inactive or infectious SARS-CoV-2 with

649    25 µg adjuvant in 50 µl made with the same ingredients as AS01 (98) as described previously (99).  A

25

650    boost was given 5-6 weeks after prime, and mice were bled to measure serum neutralizing titers 4-9

651    weeks after boost.

652

653    **Neutralization assay**

654    Mouse serum was heat inactivated at 56°C for 30 min and incubated with 100 $CCID_{50}$ SARS-CoV-2 for 2

655    hr at 37°C before adding $10^5$ Vero cells/well in a 96 well plate to 200 µl. After 4 days cells were fixed and

656    stained by adding 50 µl formaldehyde (15% w/v) and crystal violet (0.1% w/v) (Sigma-Aldrich)

657    overnight.  The plates were washed in tap water, dried overnight and 100 µl/well of 100% methanol added

658    to dissolve the crystal violet and the OD was read at 595 nm using a 96-well plate reader (Biotek Synergy

659    H4).  The 50% neutralizing titers were interpolated from optical density (OD) versus dilution plots.

660

661    **Mice intranasal lentivirus transduction and SARS-CoV-2 infection**

662    C57BL/6J, IFNAR$^{-/-}$ (100) (originally provided by P. Hertzog, Monash University, Melbourne, VIC,

663    Australia) and IL-28RA$^{-/-}$ mice (71, 101) were kindly provided by Bristol-Myers Squibb (102) and bred

664    in-house at QIMRB.  Female mice were 8 weeks to 1 year old (age matched between groups) at the start

665    of the experiment.  Mice were anesthetized using isoflurane and 4 µl of 1% L-α-Lysophosphatidylcholine

666    from egg yolk (Sigma Aldrich) in water was administered intranasally.  After 1 hour mice were inoculated

667    intranasally with approximately $2\times10^4$ TU of hACE2-pCDH lentivirus in 50 µl, and 1 week later

668    challenged with $10^5$ $CCID_{50}$ SARS-CoV-2 intranasally in 50 µl.  Mice were sacrificed by cervical

669    dislocation at day 2, 4 or 6 and lungs were collected.  Right lung was immediately homogenized in tubes

670    each containing 4 beads twice at 6000 x g for 15 seconds, and used in tissue titration as described above.

671    Left lung was placed in RNAprotect Tissue Reagent (QIAGEN) at 4°C overnight then -80°C.

672    K18-hACE2 mice (6) were purchased from The Jackson Laboratory and bred in-house at QIMRB with

673    C57BL/6J mice.  Mice were genotyped using Extract-N-Amp Tissue PCR Kit (Sigma Aldrich) according

674    to manufacturer instructions with the following primers; Forward 5'-CTTGGTGATATGTGGGGTAGA-

675    3' and Reverse 5'-CGCTTCATCTCCCACCACTT-3'.  hACE2 positive mice were infected with $5 \times 10^4$

676    SARS-CoV-2 i.n. as above and lung RNA was harvested at day 4 for RNA-seq.

677

678    **RT-qPCR**

679    Mice lung was transferred from RNAlater to TRIzol (Life Technologies) and was homogenized twice at

680    6000 x g for 15 sec.  Homogenates were centrifuged at $14,000 \times$ g for 10 min and RNA was isolated as

681    per manufacturer's instructions.  cDNA was synthesized using ProtoScript II First Strand cDNA Synthesis

682    Kit (New England Biolabs) and qPCR performed using iTaq Universal SYBR Green Supermix (Bio-Rad)

683    as per manufacturer instructions with the following primers; SARS-CoV-2 E Forward 5'-

684    ACAGGTACGTTAATAGTTAATAGCGT -3' and Reverse 5'- ATATTGCAGCAGTACGCACACA,

685    hACE2 Forward 5'- GATCACGATTCCCAGGACG -3' and Reverse 5'- TCCGGCTGAACGACAACTC

686    -3', mRPL13a (103) Forward 5'- GAGGTCGGGTGGAAGTACCA -3' and Reverse 5'-

687    TGCATCTTGGCCTTTTCCTT -3'.  PCR fragments of SARS-CoV-2 E, ACE2 and mRPL13a using the

688    same primers as above were gel purified and 10-fold serial dilutions of estimated copy numbers were used

689    as standards in qPCR to calculate copies in samples reactions.  SARS-CoV-2 E and ACE2 copies were

690    normalized by mRPL13a copy number in each reaction.  qPCR reactions were performed in duplicate and

691    averaged to determine the copy number in each sample.

692

693    **RNA-seq**

694    TRIzol extracted lung RNA was treated with DNase (RNase-Free DNAse Set (Qiagen)) followed by

695    purification using RNeasy MinElute Cleanup Kit (QIAGEN) as per manufacturer instructions.  RNA

696    concentration and quality was measured using TapeStation D1K TapeScreen assay (Agilent).  cDNA

697    libraries were prepared using the Illumina TruSeq Stranded mRNA library prep kit and the sequencing

698    performed on the Illumina Nextseq 550 platform generating 75bp paired end reads.  Per base sequence

699    quality for >90% bases was above Q30 for all samples.  The quality of raw sequencing reads was assessed

27

700    using FastQC (104) (v0.11.8) and trimmed using Cutadapt (105) (v2.3) to remove adapter sequences and

701    low-quality bases.  Trimmed reads were aligned using STAR (106) (v2.7.1a) to a combined reference that

702    included the mouse GRCm38 primary assembly and the GENCODE M23 gene model (107), SARS-CoV-

703    2 isolate Wuhan-Hu-1 (NC_045512.2; 29903 bp) and the human ACE2 mouse codon optimized sequence

704    (2418 bp).  Mouse gene expression was estimated using RSEM (108) (v1.3.0).  Reads aligned to SARS-

705    CoV-2 and hACE2 were counted using SAMtools (109) (v1.9).  Differential gene expression in the mouse

706    was analyzed using EdgeR (3.22.3) and modelled using the likelihood ratio test, glmLRT().

707

708    **Analyses of K18-hACE2 and Ad5-hACE2 RNA-seq data**

709    RNA-seq datasets generated from the Winkler et al. study (9), and Sun et al. study (43) were obtained

710    from the Gene Expression Omnibus (GSE154104 and GSE150847 respectively) and trimmed using

711    Cutadapt (v2.3).  Trimmed reads were aligned using STAR (v2.7.1a) to a combined reference that

712    included the mouse GRCm38 primary assembly and the GENCODE M23 gene model, SARS-CoV-2

713    isolate Wuhan-Hu-1 (NC_045512.2; 29903 bp) and the human ACE2 transcript variant 1

714    (NM_001371415.1; 3339 bp).  Mouse gene expression was estimated using RSEM (v1.3.0). Reads

715    aligned to SARS-CoV-2 and hACE2 were counted using SAMtools (v1.9).  Differential gene expression

716    in the mouse was analyzed using EdgeR (3.22.3) and modelled using the likelihood ratio test, glmLRT().

717

718    **Pathway Analysis**

719    Up-Stream Regulators (USR), Diseases and Functions and canonical pathways enriched in differentially

720    expressed genes in direct and indirect interactions were investigated using Ingenuity Pathway Analysis

721    (IPA) (QIAGEN).

722

723    **Network Analysis**

724    Protein interaction networks of differentially expressed gene lists were visualized in Cytoscape (v3.7.2)

725    (110).  Enrichment for biological processes, molecular functions, KEGG pathways and other gene

28

726    ontology categories in DEG lists was elucidated using the STRING database (111) and GO enrichment

727    analysis (112).

728

729    **Gene Set Enrichment Analysis**

730    Preranked GSEA (113) was performed on a desktop application (GSEA v4.0.3)

731    (http://www.broadinstitute.org/gsea/) using the "GSEAPreranked" module. Gene sets from the

732    supplemental materials from the Winkler et al. (9), Blanco-Melo et al. (51) and Wu et al. (52)

733    (filename.GMT) studies were investigated for enrichment in our pre-ranked all gene list for SARS-CoV-2

734    infected day 2 mice lung comparing plus versus minus ACE2 (Supplementary Table 2B).  Li et al. (76)

735    blood transcription modules (BTM_for_GSEA_20131008.gmt, n = 346) was also used in GSEA to

736    determine enrichment in our 'immunized' versus unvaccinated mice lung at day 2 (Supplementary Table

737    5B).  The complete Molecular Signatures Database (MSigDB) v7.2 gene set collection (31,120 gene sets)

738    (msigdb.v7.2.symbols.gmt: https://www.gsea-

739    msigdb.org/gsea/msigdb/download_file.jsp?filePath=/msigdb/release/7.2/msigdb.v7.2.symbols.gmt) was

740    used to run GSEAs on pre-ranked gene list for plus versus minus ACE2 at day 2 (Supplementary Table

741    1B), and day 6 versus day 2 (Supplementary Table 2B).  Gene ontology (114, 115) and Enrichr (116, 117)

742    web-tools were also consulted.

743

744    **Interferome**

745    The indicated DEG lists were entered into Interferome (www.interferome.org) (118) with the following

746    parameters: *In Vivo*, Mus musculus, fold change 2 (up and down).

747

748    **Statistics**

749    Statistical analyses of experimental data were performed using IBM SPSS Statistics for Windows,

750    Version 19.0 (IBM Corp., Armonk, NY, USA). The t-test was used when the difference in variances was

751    <4, skewness was >2 and kurtosis was <2. Otherwise, the non-parametric Kolmogorov–Smirnov test or

752     Kruskal-Wallis test was used.  Repeated Measures Two-Way ANOVA was used where indicated.

753

754     **SUPPPLEMENTAL INFORMATION**

755     **Supplementary Figure 1. Replication of SARS-CoV-2 in hACE2-lentivirus transduced mouse cell**

756     **lines.**  Growth kinetics of SARS-CoV-2 over a three day time course in untransduced or hACE2-lentivirus

757     transduced 3T3 or AE17 cells infected at MOI=0.1.  Data is the mean of triplicate wells and error bars

758     represent SEM.  Images of cells were taken using an inverted light microscope at day 3 post-infection and

759     are representative of triplicate wells.

760

761     **Supplementary Figure 2. RT-qPCR of mice lung RNA using primers for SARS-CoV-2 normalized**

762     **to hACE2 introduced by lentivirus transduction.**  Data is individual mice from Figure 2E normalised

763     to 2C, and is expressed as RNA copy number calculated against a standard curve for each gene.

764

765     **Supplementary Figure 3. SARS-CoV-2 and hACE2 read counts in RNA-Seq data.**  RNA-Seq was

766     performed on mice lung from the same mice as in 'Figure 2'.  **A)** SARS-CoV-2 read counts normalized to

767     total read count.  Data points below the horizontal dotted line had read counts of zero.  **B)** hACE2 read

768     counts normalised to total read count.  Data points below the horizontal dotted line had read counts of

769     zero.  **C)** SARS-CoV-2 read count normalised to hACE2 read count.  Circle with pink dotted outline had

770     hACE2 read count of 0, so the value was set to the SARS-CoV-2 read count (not normalised).  **D)** SARS-

771     CoV-2 reads aligned to reference genome viewed in Integrative Genome Viewer (IGV).  Mice with

772     hACE2 displayed reads mapped across the entire genome, with higher counts for structural gene sub-

773     genomic RNA as also evident in hACE2-adenoviral vector transduced cell lines (51).

774

775     **Supplementary Table 1.  RNA-Seq gene lists and downstream bioinformatic analyses of responses**

776     **at day 2 post-infection.**

777

778    **Supplementary Table 2.  RNA-Seq gene lists and downstream bioinformatic analyses of responses**

779    **at day 6 post-infection.**

780

781    **Supplementary Table 3.  RNA-Seq gene lists and downstream bioinformatic analyses of responses**

782    **in IFNAR$^{-/-}$ versus C57BL/6J mice at day 2 post-infection.**

783

784    **Supplementary Table 4.  RNA-Seq gene lists and downstream bioinformatic analyses of responses**

785    **in IL-28RA$^{-/-}$ versus C57BL/6J mice at day 2 post-infection.**

786

787    **Supplementary Table 5.  RNA-Seq gene lists and downstream bioinformatic analyses of responses**

788    **in immunized versus unvaccinated mice at day 2 post-infection.**

789

790    **REFERENCES**

791

792    1.      Wu F, Zhao S, Yu B, Chen Y-M, Wang W, Song Z-G, et al. A new coronavirus associated with
793    human respiratory disease in China. Nature. 2020;579(7798):265-9. doi: 10.1038/s41586-020-2008-3.
794    2.      Guan W-j, Ni Z-y, Hu Y, Liang W-h, Ou C-q, He J-x, et al. Clinical Characteristics of Coronavirus
795    Disease 2019 in China. New England Journal of Medicine. 2020;382(18):1708-20. doi:
796    10.1056/NEJMoa2002032.
797    3.      Muñoz-Fontela C, Dowling WE, Funnell SGP, Gsell P-S, Riveros-Balta AX, Albrecht RA, et al.
798    Animal models for COVID-19. Nature. 2020;586(7830):509-15. doi: 10.1038/s41586-020-2787-6.
799    4.      Zhao X, Chen D, Szabla R, Zheng M, Li G, Du P, et al. Broad and Differential Animal Angiotensin-
800    Converting Enzyme 2 Receptor Usage by SARS-CoV-2. Journal of virology. 2020;94(18). doi:
801    10.1128/jvi.00940-20.
802    5.      Zhou P, Yang X-L, Wang X-G, Hu B, Zhang L, Zhang W, et al. A pneumonia outbreak associated
803    with a new coronavirus of probable bat origin. Nature. 2020;579(7798):270-3. doi: 10.1038/s41586-020-
804    2012-7.
805    6.      McCray PB, Jr., Pewe L, Wohlford-Lenane C, Hickey M, Manzel L, Shi L, et al. Lethal infection of
806    K18-hACE2 mice infected with severe acute respiratory syndrome coronavirus. Journal of virology.
807    2007;81(2):813-21. doi: 10.1128/jvi.02012-06.
808    7.      Golden JW, Cline CR, Zeng X, Garrison AR, Carey BD, Mucker EM, et al. Human angiotensin-
809    converting enzyme 2 transgenic mice infected with SARS-CoV-2 develop severe and fatal respiratory
810    disease. JCI insight. 2020. doi: 10.1172/jci.insight.142032.

31

811    8.       Moreau GB, Burgess SL, Sturek JM, Donlan AN, Petri WA, Mann BJ. Evaluation of K18-hACE2
812    Mice as a Model of SARS-CoV-2 Infection. The American journal of tropical medicine and hygiene.
813    2020;103(3):1215-9. doi: 10.4269/ajtmh.20-0762.
814    9.       Winkler ES, Bailey AL, Kafai NM, Nair S, McCune BT, Yu J, et al. SARS-CoV-2 infection of human
815    ACE2-transgenic mice causes severe lung inflammation and impaired function. Nature immunology.
816    2020. doi: 10.1038/s41590-020-0778-2.
817    10.      Rathnasinghe R, Strohmeier S, Amanat F, Gillespie VL, Krammer F, García-Sastre A, et al.
818    Comparison of Transgenic and Adenovirus hACE2 Mouse Models for SARS-CoV-2 Infection. Emerging
819    microbes & infections. 2020:1-19. doi: 10.1080/22221751.2020.1838955.
820    11.      Oladunni FS, Park J-G, Pino PA, Gonzalez O, Akhter A, Allué-Guardia A, et al. Lethality of SARS-
821    CoV-2 infection in K18 human angiotensin-converting enzyme 2 transgenic mice. Nature
822    Communications. 2020;11(1):6122. doi: 10.1038/s41467-020-19891-7.
823    12.      Yinda CK, Port JR, Bushmaker T, Offei Owusu I, Purushotham JN, Avanzato VA, et al. K18-hACE2
824    mice develop respiratory disease resembling severe COVID-19. PLoS Pathog. 2021;17(1):e1009195. doi:
825    10.1371/journal.ppat.1009195.
826    13.      Bao L, Deng W, Huang B, Gao H, Liu J, Ren L, et al. The pathogenicity of SARS-CoV-2 in hACE2
827    transgenic mice. Nature. 2020;583(7818):830-3. doi: 10.1038/s41586-020-2312-y.
828    14.      Sun SH, Chen Q, Gu HJ, Yang G, Wang YX, Huang XY, et al. A Mouse Model of SARS-CoV-2
829    Infection and Pathogenesis. Cell host & microbe. 2020;28(1):124-33.e4. doi:
830    10.1016/j.chom.2020.05.020.
831    15.      Jiang R-D, Liu M-Q, Chen Y, Shan C, Zhou Y-W, Shen X-R, et al. Pathogenesis of SARS-CoV-2 in
832    Transgenic Mice Expressing Human Angiotensin-Converting Enzyme 2. Cell. 2020;182(1):50-8.e8. doi:
833    10.1016/j.cell.2020.05.027.
834    16.      Tseng CT, Huang C, Newman P, Wang N, Narayanan K, Watts DM, et al. Severe acute respiratory
835    syndrome coronavirus infection of mice transgenic for the human Angiotensin-converting enzyme 2
836    virus receptor. Journal of virology. 2007;81(3):1162-73. doi: 10.1128/jvi.01702-06.
837    17.      Hassan AO, Case JB, Winkler ES, Thackray LB, Kafai NM, Bailey AL, et al. A SARS-CoV-2 Infection
838    Model in Mice Demonstrates Protection by Neutralizing Antibodies. Cell. 2020;182(3):744-53.e4. doi:
839    https://doi.org/10.1016/j.cell.2020.06.011.
840    18.      Israelow B, Song E, Mao T, Lu P, Meir A, Liu F, et al. Mouse model of SARS-CoV-2 reveals
841    inflammatory role of type I interferon signaling. The Journal of experimental medicine. 2020;217(12).
842    doi: 10.1084/jem.20201241.
843    19.      Leist SR, Dinnon KH, 3rd, Schäfer A, Tse LV, Okuda K, Hou YJ, et al. A Mouse-Adapted SARS-CoV-2
844    Induces Acute Lung Injury and Mortality in Standard Laboratory Mice. Cell. 2020. doi:
845    10.1016/j.cell.2020.09.050.
846    20.      Dinnon KH, Leist SR, Schäfer A, Edwards CE, Martinez DR, Montgomery SA, et al. A mouse-
847    adapted model of SARS-CoV-2 to test COVID-19 countermeasures. Nature. 2020;586(7830):560-6. doi:
848    10.1038/s41586-020-2708-8.
849    21.      Gu H, Chen Q, Yang G, He L, Fan H, Deng Y-Q, et al. Adaptation of SARS-CoV-2 in BALB/c mice for
850    testing vaccine efficacy. Science (New York, NY). 2020;369(6511):1603-7. doi: 10.1126/science.abc4730.
851    22.      Copreni E, Palmieri L, Castellani S, Conese M. A VSV-G Pseudotyped Last Generation Lentiviral
852    Vector Mediates High Level and Persistent Gene Transfer in Models of Airway Epithelium In Vitro and In
853    Vivo. Viruses. 2010;2(8):1577-88. doi: 10.3390/v2081577.
854    23.      Limberis MP, Bell CL, Heath J, Wilson JM. Activation of transgene-specific T cells following
855    lentivirus-mediated gene delivery to mouse lung. Mol Ther. 2010;18(1):143-50. doi:
856    10.1038/mt.2009.190.
857    24.      Wilson JM. Adeno-associated virus and lentivirus pseudotypes for lung-directed gene therapy.
858    Proceedings of the American Thoracic Society. 2004;1(4):309-14. doi: 10.1513/pats.200409-041MS.

859    25.    Kremer KL, Dunning KR, Parsons DW, Anson DS. Gene delivery to airway epithelial cells in vivo: a
860    direct comparison of apical and basolateral transduction strategies using pseudotyped lentivirus vectors.
861    The journal of gene medicine. 2007;9(5):362-8. doi: 10.1002/jgm.1025.
862    26.    Buckley SMK, Howe SJ, Sheard V, Ward NJ, Coutelle C, Thrasher AJ, et al. Lentiviral transduction
863    of the murine lung provides efficient pseudotype and developmental stage-dependent cell-specific
864    transgene expression. Gene Therapy. 2008;15(16):1167-75. doi: 10.1038/gt.2008.74.
865    27.    Copreni E, Penzo M, Carrabino S, Conese M. Lentivirus-mediated gene transfer to the respiratory
866    epithelium: a promising approach to gene therapy of cystic fibrosis. Gene Therapy. 2004;11(1):S67-S75.
867    doi: 10.1038/sj.gt.3302372.
868    28.    Alton EWFW, Beekman JM, Boyd AC, Brand J, Carlon MS, Connolly MM, et al. Preparation for a
869    first-in-man lentivirus trial in patients with cystic fibrosis. Thorax. 2017;72(2):137. doi:
870    10.1136/thoraxjnl-2016-208406.
871    29.    Alton EW, Beekman JM, Boyd AC, Brand J, Carlon MS, Connolly MM, et al. Preparation for a first-
872    in-man lentivirus trial in patients with cystic fibrosis. Thorax. 2017;72(2):137-47. doi: 10.1136/thoraxjnl-
873    2016-208406.
874    30.    Crawford KHD, Eguia R, Dingens AS, Loes AN, Malone KD, Wolf CR, et al. Protocol and Reagents
875    for Pseudotyping Lentiviral Particles with SARS-CoV-2 Spike Protein for Neutralization Assays. Viruses.
876    2020;12(5). doi: 10.3390/v12050513.
877    31.    Chan KK, Dorosky D, Sharma P, Abbasi SA, Dye JM, Kranz DM, et al. Engineering human ACE2 to
878    optimize binding to the spike protein of SARS coronavirus 2. Science (New York, NY).
879    2020;369(6508):1261-5. doi: 10.1126/science.abc0870.
880    32.    Mehdipour AR, Hummer G. Dual nature of human ACE2 glycosylation in binding to SARS-CoV-2
881    spike. bioRxiv. 2020:2020.07.09.193680. doi: 10.1101/2020.07.09.193680.
882    33.    Wang Q, Zhang Y, Wu L, Niu S, Song C, Zhang Z, et al. Structural and Functional Basis of SARS-
883    CoV-2 Entry by Using Human ACE2. Cell. 2020;181(4):894-904.e9. doi:
884    https://doi.org/10.1016/j.cell.2020.03.045.
885    34.    Rodrigues JPGLM, Barrera-Vilarmau S, M. C. Teixeira J, Sorokina M, Seckel E, Kastritis PL, et al.
886    Insights on cross-species transmission of SARS-CoV-2 from structural modeling. PLOS Computational
887    Biology. 2020;16(12):e1008449. doi: 10.1371/journal.pcbi.1008449.
888    35.    Griffin BD, Chan M, Tailor N, Mendoza EJ, Leung A, Warner BM, et al. North American deer mice
889    are susceptible to SARS-CoV-2. bioRxiv. 2020:2020.07.25.221291. doi: 10.1101/2020.07.25.221291.
890    36.    Alexander MR, Schoeder CT, Brown JA, Smart CD, Moth C, Wikswo JP, et al. Predicting
891    susceptibility to SARS-CoV-2 infection based on structural differences in ACE2 across species. The FASEB
892    Journal. 2020;34(12):15946-60. doi: https://doi.org/10.1096/fj.202001808R.
893    37.    Damas J, Hughes GM, Keough KC, Painter CA, Persky NS, Corbo M, et al. Broad host range of
894    SARS-CoV-2 predicted by comparative and structural analysis of ACE2 in vertebrates. Proceedings of the
895    National Academy of Sciences. 2020;117(36):22311-22. doi: 10.1073/pnas.2010146117.
896    38.    Plante JA, Mitchell BM, Plante KS, Debbink K, Weaver SC, Menachery VD. The Variant Gambit:
897    COVID's Next Move. Cell host & microbe. doi: 10.1016/j.chom.2021.02.020.
898    39.    Starr TN, Greaney AJ, Addetia A, Hannon WW, Choudhary MC, Dingens AS, et al. Prospective
899    mapping of viral mutations that escape antibodies used to treat COVID-19. Science (New York, NY).
900    2021;371(6531):850-4. doi: 10.1126/science.abf9302.
901    40.    Greaney AJ, Starr TN, Gilchuk P, Zost SJ, Binshtein E, Loes AN, et al. Complete Mapping of
902    Mutations to the SARS-CoV-2 Spike Receptor-Binding Domain that Escape Antibody Recognition. Cell
903    host & microbe. 2021;29(1):44-57.e9. doi: 10.1016/j.chom.2020.11.007.
904    41.    Sun S, Gu H, Cao L, Chen Q, Yang G, Li R-T, et al. Characterization and structural basis of a lethal
905    mouse-adapted SARS-CoV-2. bioRxiv. 2020:2020.11.10.377333. doi: 10.1101/2020.11.10.377333.

906    42.    Limberis M, Anson DS, Fuller M, Parsons DW. Recovery of airway cystic fibrosis transmembrane
907    conductance regulator function in mice with cystic fibrosis after single-dose lentivirus-mediated gene
908    transfer. Human gene therapy. 2002;13(16):1961-70. doi: 10.1089/10430340260355365.
909    43.    Sun J, Zhuang Z, Zheng J, Li K, Wong RL-Y, Liu D, et al. Generation of a Broadly Useful Model for
910    COVID-19 Pathogenesis, Vaccination, and Treatment. Cell. 2020;182(3):734-43.e5. doi:
911    https://doi.org/10.1016/j.cell.2020.06.010.
912    44.    Jefferson T, Spencer E, Brassey J, Heneghan C. Viral cultures for COVID-19 infectivity assessment.
913    Systematic review. medRxiv. 2020:2020.08.04.20167932. doi: 10.1101/2020.08.04.20167932.
914    45.    Weiskopf D, Schmitz KS, Raadsen MP, Grifoni A, Okba NMA, Endeman H, et al. Phenotype and
915    kinetics of SARS-CoV-2–specific T cells in COVID-19 patients with acute respiratory distress syndrome.
916    Science Immunology. 2020;5(48):eabd2071. doi: 10.1126/sciimmunol.abd2071.
917    46.    Channappanavar R, Fehr Anthony R, Vijay R, Mack M, Zhao J, Meyerholz David K, et al.
918    Dysregulated Type I Interferon and Inflammatory Monocyte-Macrophage Responses Cause Lethal
919    Pneumonia in SARS-CoV-Infected Mice. Cell host & microbe. 2016;19(2):181-93. doi:
920    https://doi.org/10.1016/j.chom.2016.01.007.
921    47.    Pence BD. Severe COVID-19 and aging: are monocytes the key? Geroscience. 2020;42(4):1051-
922    61. doi: 10.1007/s11357-020-00213-0.
923    48.    Banerjee AK, Blanco MR, Bruce EA, Honson DD, Chen LM, Chow A, et al. SARS-CoV-2 Disrupts
924    Splicing, Translation, and Protein Trafficking to Suppress Host Defenses. Cell. 2020;183(5):1325-39.e21.
925    doi: https://doi.org/10.1016/j.cell.2020.10.004.
926    49.    Schubert K, Karousis ED, Jomaa A, Scaiola A, Echeverria B, Gurzeler L-A, et al. SARS-CoV-2 Nsp1
927    binds the ribosomal mRNA channel to inhibit translation. Nature Structural & Molecular Biology.
928    2020;27(10):959-66. doi: 10.1038/s41594-020-0511-8.
929    50.    Miller B, Silverstein A, Flores M, Cao K, Kumagai H, Mehta HH, et al. Host mitochondrial
930    transcriptome response to SARS-CoV-2 in multiple cell models and clinical samples. Scientific Reports.
931    2021;11(1):3. doi: 10.1038/s41598-020-79552-z.
932    51.    Blanco-Melo D, Nilsson-Payant BE, Liu WC, Uhl S, Hoagland D, Møller R, et al. Imbalanced Host
933    Response to SARS-CoV-2 Drives Development of COVID-19. Cell. 2020;181(5):1036-45.e9. doi:
934    10.1016/j.cell.2020.04.026.
935    52.    Wu M, Chen Y, Xia H, Wang C, Tan CY, Cai X, et al. Transcriptional and proteomic insights into the
936    host response in fatal COVID-19 cases. Proceedings of the National Academy of Sciences.
937    2020;117(45):28336. doi: 10.1073/pnas.2018030117.
938    53.    Vaz de Paula CB, de Azevedo MLV, Nagashima S, Martins APC, Malaquias MAS, Miggiolaro
939    AFRdS, et al. IL-4/IL-13 remodeling pathway of COVID-19 lung injury. Scientific Reports.
940    2020;10(1):18689. doi: 10.1038/s41598-020-75659-5.
941    54.    Lavoie H, Gagnon J, Therrien M. ERK signalling: a master regulator of cell behaviour, life and fate.
942    Nature Reviews Molecular Cell Biology. 2020;21(10):607-32. doi: 10.1038/s41580-020-0255-7.
943    55.    Sountoulidis A, Stavropoulos A, Giaglis S, Apostolou E, Monteiro R, Chuva de Sousa Lopes SM, et
944    al. Activation of the Canonical Bone Morphogenetic Protein (BMP) Pathway during Lung Morphogenesis
945    and Adult Lung Tissue Repair. PLOS ONE. 2012;7(8):e41460. doi: 10.1371/journal.pone.0041460.
946    56.    Zhu Y, Wang W, Wang X. Roles of transcriptional factor 7 in production of inflammatory factors
947    for lung diseases. J Transl Med. 2015;13:273-. doi: 10.1186/s12967-015-0617-7.
948    57.    Lin L, Han Q, Xiong Y, Li T, Liu Z, Xu H, et al. Krüpple-like-factor 4 Attenuates Lung Fibrosis via
949    Inhibiting Epithelial-mesenchymal Transition. Scientific reports. 2017;7(1):15847-. doi: 10.1038/s41598-
950    017-14602-7.
951    58.    Raslan AA, Yoon JK. WNT Signaling in Lung Repair and Regeneration. Mol Cells. 2020;43(9):774-
952    83. doi: 10.14348/molcells.2020.0059.

953    59.      Wang H, Kadlecek TA, Au-Yeung BB, Goodfellow HES, Hsu L-Y, Freedman TS, et al. ZAP-70: an
954    essential kinase in T-cell signaling. Cold Spring Harb Perspect Biol. 2010;2(5):a002279-a. doi:
955    10.1101/cshperspect.a002279.
956    60.      Nechanitzky R, Akbas D, Scherer S, Györy I, Hoyler T, Ramamoorthy S, et al. Transcription factor
957    EBF1 is essential for the maintenance of B cell identity and prevention of alternative fates in committed
958    cells. Nature immunology. 2013;14(8):867-75. doi: 10.1038/ni.2641.
959    61.      Duperray C, Boiron JM, Boucheix C, Cantaloube JF, Lavabre-Bertrand T, Attal M, et al. The CD24
960    antigen discriminates between pre-B and B cells in human bone marrow. J Immunol. 1990;145(11):3678-
961    83. doi:
962    62.      Curtin N, Bányai K, Thaventhiran J, Le Quesne J, Helyes Z, Bai P. Repositioning PARP inhibitors for
963    SARS-CoV-2 infection(COVID-19); a new multi-pronged therapy for acute respiratory distress syndrome?
964    British Journal of Pharmacology. 2020;177(16):3635-45. doi: https://doi.org/10.1111/bph.15137.
965    63.      Badawy AAB. Immunotherapy of COVID-19 with poly (ADP-ribose) polymerase inhibitors:
966    starting with nicotinamide. Biosci Rep. 2020;40(10):BSR20202856. doi: 10.1042/BSR20202856.
967    64.      Pinna G. Sex and COVID-19: A Protective Role for Reproductive Steroids. Trends in endocrinology
968    and metabolism: TEM. 2021;32(1):3-6. doi: 10.1016/j.tem.2020.11.004.
969    65.      Peckham H, de Gruijter NM, Raine C, Radziszewska A, Ciurtin C, Wedderburn LR, et al. Male sex
970    identified by global COVID-19 meta-analysis as a risk factor for death and ITU admission. Nature
971    Communications. 2020;11(1):6317. doi: 10.1038/s41467-020-19741-6.
972    66.      Jin J-M, Bai P, He W, Wu F, Liu X-F, Han D-M, et al. Gender Differences in Patients With COVID-
973    19: Focus on Severity and Mortality. Frontiers in Public Health. 2020;8(152). doi:
974    10.3389/fpubh.2020.00152.
975    67.      Channappanavar R, Fett C, Mack M, Ten Eyck PP, Meyerholz DK, Perlman S. Sex-Based
976    Differences in Susceptibility to Severe Acute Respiratory Syndrome Coronavirus Infection. J Immunol.
977    2017;198(10):4046-53. doi: 10.4049/jimmunol.1601896.
978    68.      Nicks KM, Fowler TW, Akel NS, Perrien DS, Suva LJ, Gaddy D. Bone turnover across the
979    menopause transition : The role of gonadal inhibins. Ann N Y Acad Sci. 2010;1192:153-60. doi:
980    10.1111/j.1749-6632.2009.05349.x.
981    69.      Frieman MB, Chen J, Morrison TE, Whitmore A, Funkhouser W, Ward JM, et al. SARS-CoV
982    Pathogenesis Is Regulated by a STAT1 Dependent but a Type I, II and III Interferon Receptor Independent
983    Mechanism. PLOS Pathogens. 2010;6(4):e1000849. doi: 10.1371/journal.ppat.1000849.
984    70.      Lazear HM, Schoggins JW, Diamond MS. Shared and Distinct Functions of Type I and Type III
985    Interferons. Immunity. 2019;50(4):907-23. doi: 10.1016/j.immuni.2019.03.025.
986    71.      Galani IE, Triantafyllia V, Eleminiadou EE, Koltsida O, Stavropoulos A, Manioudaki M, et al.
987    Interferon-λ Mediates Non-redundant Front-Line Antiviral Protection against Influenza Virus Infection
988    without Compromising Host Fitness. Immunity. 2017;46(5):875-90.e6. doi:
989    10.1016/j.immuni.2017.04.025.
990    72.      Vanderheiden A, Ralfs P, Chirkova T, Upadhyay AA, Zimmerman MG, Bedoya S, et al. Type I and
991    Type III Interferons Restrict SARS-CoV-2 Infection of Human Airway Epithelial Cultures. Journal of
992    virology. 2020;94(19):e00985-20. doi: 10.1128/JVI.00985-20.
993    73.      Boudewijns R, Thibaut HJ, Kaptein SJF, Li R, Vergote V, Seldeslachts L, et al. STAT2 signaling
994    restricts viral dissemination but drives severe pneumonia in SARS-CoV-2 infected hamsters. Nature
995    Communications. 2020;11(1):5838. doi: 10.1038/s41467-020-19684-y.
996    74.      Takasuka N, Fujii H, Takahashi Y, Kasai M, Morikawa S, Itamura S, et al. A subcutaneously
997    injected UV-inactivated SARS coronavirus vaccine elicits systemic humoral immunity in mice.
998    International immunology. 2004;16(10):1423-30. doi: 10.1093/intimm/dxh143.

999    75.     Wajnberg A, Amanat F, Firpo A, Altman DR, Bailey MJ, Mansour M, et al. Robust neutralizing
1000    antibodies to SARS-CoV-2 infection persist for months. Science (New York, NY). 2020;370(6521):1227.
1001    doi: 10.1126/science.abd7728.
1002    76.     Li S, Rouphael N, Duraisingham S, Romero-Steiner S, Presnell S, Davis C, et al. Molecular
1003    signatures of antibody responses derived from a systems biology study of five human vaccines. Nature
1004    immunology. 2014;15(2):195-204. doi: 10.1038/ni.2789.
1005    77.     Tan AT, Linster M, Tan CW, Le Bert N, Chia WN, Kunasegaran K, et al. Early induction of
1006    functional SARS-CoV-2-specific T cells associates with rapid viral clearance and mild disease in COVID-19
1007    patients. Cell Reports. 2021;34(6):108728. doi: https://doi.org/10.1016/j.celrep.2021.108728.
1008    78.     Kumari P, Rothan HA, Natekar JP, Stone S, Pathak H, Strate PG, et al. Neuroinvasion and
1009    encephalitis following intranasal inoculation of SARS-CoV-2 in K18-hACE2 mice. bioRxiv.
1010    2020:2020.12.14.422714. doi: 10.1101/2020.12.14.422714.
1011    79.     Carossino M, Montanaro P, O'Connell A, Kenney D, Gertje H, Grosz KA, et al. Fatal neuroinvasion
1012    of SARS-CoV-2 in K18-hACE2 mice is partially dependent on hACE2 expression. bioRxiv. 2021. doi:
1013    10.1101/2021.01.13.425144.
1014    80.     Huang C, Wang Y, Li X, Ren L, Zhao J, Hu Y, et al. Clinical features of patients infected with 2019
1015    novel coronavirus in Wuhan, China. Lancet (London, England). 2020;395(10223):497-506. doi:
1016    10.1016/s0140-6736(20)30183-5.
1017    81.     Han H, Ma Q, Li C, Liu R, Zhao L, Wang W, et al. Profiling serum cytokines in COVID-19 patients
1018    reveals IL-6 and IL-10 are disease severity predictors. Emerging microbes & infections. 2020;9(1):1123-
1019    30. doi: 10.1080/22221751.2020.1770129.
1020    82.     Herold T, Jurinovic V, Arnreich C, Lipworth BJ, Hellmuth JC, von Bergwelt-Baildon M, et al.
1021    Elevated levels of IL-6 and CRP predict the need for mechanical ventilation in COVID-19. Journal of
1022    Allergy and Clinical Immunology. 2020;146(1):128-36.e4. doi: https://doi.org/10.1016/j.jaci.2020.05.008.
1023    83.     Xia H, Cao Z, Xie X, Zhang X, Chen JY-C, Wang H, et al. Evasion of Type I Interferon by SARS-CoV-
1024    2. Cell Reports. 2020;33(1):108234. doi: https://doi.org/10.1016/j.celrep.2020.108234.
1025    84.     Masiá M, Fernández-González M, Padilla S, Ortega P, García JA, Agulló V, et al. Impact of
1026    interleukin-6 blockade with tocilizumab on SARS-CoV-2 viral kinetics and antibody responses in patients
1027    with COVID-19: A prospective cohort study. EBioMedicine. 2020;60. doi: 10.1016/j.ebiom.2020.102999.
1028    85.     Lu L, Zhang H, Dauphars DJ, He Y-W. A Potential Role of Interleukin 10 in COVID-19 Pathogenesis.
1029    Trends in Immunology. 2021;42(1):3-5. doi: https://doi.org/10.1016/j.it.2020.10.012.
1030    86.     Gadotti AC, de Castro Deus M, Telles JP, Wind R, Goes M, Garcia Charello Ossoski R, et al. IFN-γ is
1031    an independent risk factor associated with mortality in patients with moderate and severe COVID-19
1032    infection. Virus Res. 2020;289:198171-. doi: 10.1016/j.virusres.2020.198171.
1033    87.     Mahlakõiv T, Ritz D, Mordstein M, DeDiego ML, Enjuanes L, Müller MA, et al. Combined action of
1034    type I and type III interferon restricts initial replication of severe acute respiratory syndrome coronavirus
1035    in the lung but fails to inhibit systemic virus spread. The Journal of general virology. 2012;93(Pt
1036    12):2601-5. doi: 10.1099/vir.0.046284-0.
1037    88.     Felgenhauer U, Schoen A, Gad HH, Hartmann R, Schaubmar AR, Failing K, et al. Inhibition of
1038    SARS-CoV-2 by type I and type III interferons. J Biol Chem. 2020;295(41):13958-64. doi:
1039    10.1074/jbc.AC120.013788.
1040    89.     Nguyen TH, McAuley JL, Kim Y, Zheng MZ, Gherardin NA, Godfrey DI, et al. Influenza, but not
1041    SARS-CoV-2, infection induces a rapid interferon response that wanes with age and diminished tissue-
1042    resident memory CD8(+) T cells. Clin Transl Immunology. 2021;10(1):e1242-e. doi: 10.1002/cti2.1242.
1043    90.     Jiang H-w, Zhang H-n, Meng Q-f, Xie J, Li Y, Chen H, et al. SARS-CoV-2 Orf9b suppresses type I
1044    interferon responses by targeting TOM70. Cellular & Molecular Immunology. 2020;17(9):998-1000. doi:
1045    10.1038/s41423-020-0514-8.

1046    91.    Miorin L, Kehrer T, Sanchez-Aparicio MT, Zhang K, Cohen P, Patel RS, et al. SARS-CoV-2 Orf6
1047    hijacks Nup98 to block STAT nuclear import and antagonize interferon signaling. Proceedings of the
1048    National Academy of Sciences. 2020;117(45):28344. doi: 10.1073/pnas.2016650117.
1049    92.    Hall JC, Rosen A. Type I interferons: crucial participants in disease amplification in autoimmunity.
1050    Nat Rev Rheumatol. 2010;6(1):40-9. doi: 10.1038/nrrheum.2009.237.
1051    93.    Monk PD, Marsden RJ, Tear VJ, Brookes J, Batten TN, Mankowski M, et al. Safety and efficacy of
1052    inhaled nebulised interferon beta-1a (SNG001) for treatment of SARS-CoV-2 infection: a randomised,
1053    double-blind, placebo-controlled, phase 2 trial. The Lancet Respiratory Medicine. 2020. doi:
1054    https://doi.org/10.1016/S2213-2600(20)30511-7.
1055    94.    Park A, Iwasaki A. Type I and Type III Interferons - Induction, Signaling, Evasion, and Application
1056    to Combat COVID-19. Cell host & microbe. 2020;27(6):870-8. doi: 10.1016/j.chom.2020.05.008.
1057    95.    Lan J, Ge J, Yu J, Shan S, Zhou H, Fan S, et al. Structure of the SARS-CoV-2 spike receptor-binding
1058    domain bound to the ACE2 receptor. Nature. 2020;581(7807):215-20. doi: 10.1038/s41586-020-2180-5.
1059    96.    Johnson BJ, Le TT, Dobbin CA, Banovic T, Howard CB, Flores Fde M, et al. Heat shock protein 10
1060    inhibits lipopolysaccharide-induced inflammatory mediator production. J Biol Chem. 2005;280(6):4037-
1061    47. doi: M411569200 [pii]

1062    10.1074/jbc.M411569200.
1063    97.    La Linn M, Bellett AJ, Parsons PG, Suhrbier A. Complete removal of mycoplasma from viral
1064    preparations using solvent extraction. J Virol Methods. 1995;52(1-2):51-4. doi:
1065    98.    Chlibek R, Bayas JM, Collins H, de la Pinta MLR, Ledent E, Mols JF, et al. Safety and
1066    Immunogenicity of an AS01-adjuvanted Varicella-zoster Virus Subunit Candidate Vaccine Against Herpes
1067    Zoster in Adults ≥50 Years of Age. The Journal of Infectious Diseases. 2013;208(12):1953-61. doi:
1068    10.1093/infdis/jit365.
1069    99.    Yan K, Vet LJ, Tang B, Hobson-Peters J, Rawle DJ, Le TT, et al. A Yellow Fever Virus 17D Infection
1070    and Disease Mouse Model Used to Evaluate a Chimeric Binjari-Yellow Fever Virus Vaccine. Vaccines.
1071    2020;8(3). doi: 10.3390/vaccines8030368.
1072    100.    Swann JB, Hayakawa Y, Zerafa N, Sheehan KC, Scott B, Schreiber RD, et al. Type I IFN contributes
1073    to NK cell homeostasis, activation, and antitumor function. J Immunol. 2007;178(12):7540-9. doi:
1074    10.4049/jimmunol.178.12.7540.
1075    101.    Ank N, Iversen MB, Bartholdy C, Staeheli P, Hartmann R, Jensen UB, et al. An Important Role for
1076    Type III Interferon (IFN-λ/IL-28) in TLR-Induced Antiviral Activity. The Journal of Immunology.
1077    2008;180(4):2474-85. doi: 10.4049/jimmunol.180.4.2474.
1078    102.    Souza-Fonseca-Guimaraes F, Young A, Mittal D, Martinet L, Bruedigam C, Takeda K, et al. NK cells
1079    require IL-28R for optimal in vivo activity. Proc Natl Acad Sci U S A. 2015;112(18):E2376-84. doi:
1080    10.1073/pnas.1424241112.
1081    103.    Schroder WA, Le TTT, Major L, Street S, Gardner J, Lambley E, et al. A Physiological Function of
1082    Inflammation-Associated SerpinB2 Is Regulation of Adaptive Immunity. The Journal of Immunology.
1083    2010;184(5):2663. doi: 10.4049/jimmunol.0902187.
1084    104.    Simons A. A quality control tool for high throughput sequence data. Available online:
1085    https://www.bioinformatics.babraham.ac.uk/projects/fastqc. 2010. doi:
1086    105.    Martin M. Cutadapt removes adapter sequences from high-throughput sequencing reads. 2011.
1087    2011;17(1):3. doi: 10.14806/ej.17.1.200.
1088    106.    Dobin A, Davis CA, Schlesinger F, Drenkow J, Zaleski C, Jha S, et al. STAR: ultrafast universal RNA-
1089    seq aligner. Bioinformatics. 2013;29(1):15-21. doi: 10.1093/bioinformatics/bts635.
1090    107.    Harrow J, Frankish A, Gonzalez JM, Tapanari E, Diekhans M, Kokocinski F, et al. GENCODE: the
1091    reference human genome annotation for The ENCODE Project. Genome Res. 2012;22(9):1760-74. doi:
1092    10.1101/gr.135350.111.

1093    108.    Li B, Dewey CN. RSEM: accurate transcript quantification from RNA-Seq data with or without a
1094    reference genome. BMC Bioinformatics. 2011;12(1):323. doi: 10.1186/1471-2105-12-323.
1095    109.    Li H, Handsaker B, Wysoker A, Fennell T, Ruan J, Homer N, et al. The Sequence Alignment/Map
1096    format and SAMtools. Bioinformatics. 2009;25(16):2078-9. doi: 10.1093/bioinformatics/btp352.
1097    110.    Shannon P, Markiel A, Ozier O, Baliga NS, Wang JT, Ramage D, et al. Cytoscape: a software
1098    environment for integrated models of biomolecular interaction networks. Genome Res.
1099    2003;13(11):2498-504. doi: 10.1101/gr.1239303.
1100    111.    Szklarczyk D, Gable AL, Lyon D, Junge A, Wyder S, Huerta-Cepas J, et al. STRING v11: protein-
1101    protein association networks with increased coverage, supporting functional discovery in genome-wide
1102    experimental datasets. Nucleic acids research. 2019;47(D1):D607-D13. doi: 10.1093/nar/gky1131.
1103    112.    Mi H, Muruganujan A, Ebert D, Huang X, Thomas PD. PANTHER version 14: more genomes, a
1104    new PANTHER GO-slim and improvements in enrichment analysis tools. Nucleic Acids Res.
1105    2019;47(D1):D419-d26. doi: 10.1093/nar/gky1038.
1106    113.    Subramanian A, Tamayo P, Mootha VK, Mukherjee S, Ebert BL, Gillette MA, et al. Gene set
1107    enrichment analysis: a knowledge-based approach for interpreting genome-wide expression profiles.
1108    Proc Natl Acad Sci U S A. 2005;102(43):15545-50. doi: 10.1073/pnas.0506580102.
1109    114.    Ashburner M, Ball CA, Blake JA, Botstein D, Butler H, Cherry JM, et al. Gene ontology: tool for the
1110    unification of biology. The Gene Ontology Consortium. Nature genetics. 2000;25(1):25-9. doi:
1111    10.1038/75556.
1112    115.    Consortium GO. The Gene Ontology resource: enriching a GOld mine. Nucleic Acids Res.
1113    2021;49(D1):D325-d34. doi: 10.1093/nar/gkaa1113.
1114    116.    Chen EY, Tan CM, Kou Y, Duan Q, Wang Z, Meirelles GV, et al. Enrichr: interactive and
1115    collaborative HTML5 gene list enrichment analysis tool. BMC Bioinformatics. 2013;14:128. doi:
1116    10.1186/1471-2105-14-128.
1117    117.    Kuleshov MV, Jones MR, Rouillard AD, Fernandez NF, Duan Q, Wang Z, et al. Enrichr: a
1118    comprehensive gene set enrichment analysis web server 2016 update. Nucleic Acids Res.
1119    2016;44(W1):W90-7. doi: 10.1093/nar/gkw377.
1120    118.    Rusinova I, Forster S, Yu S, Kannan A, Masse M, Cumming H, et al. INTERFEROME v2.0: an
1121    updated database of annotated interferon-regulated genes. Nucleic Acids Research. 2013;41(D1):D1040-
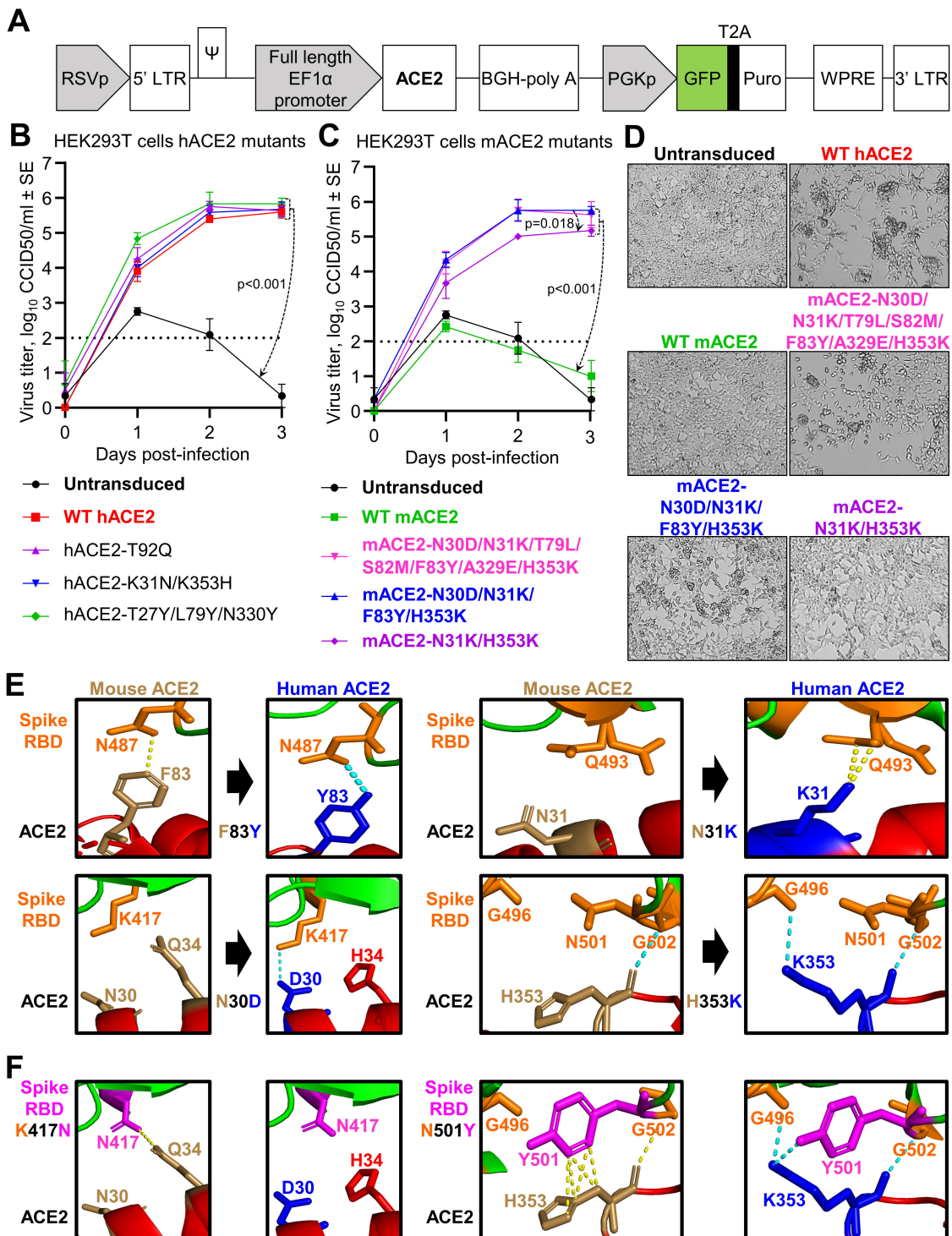1122    D6. doi: 10.1093/nar/gks1215.
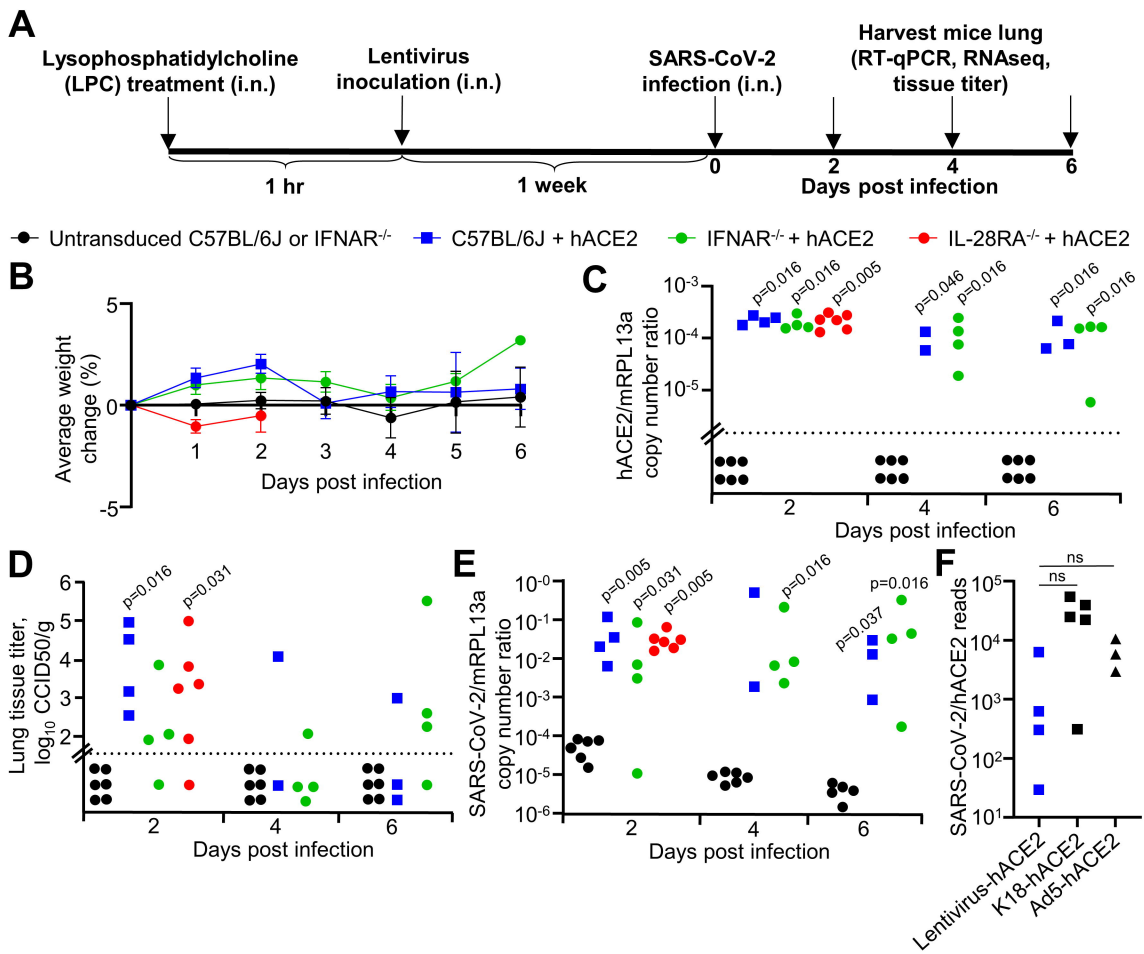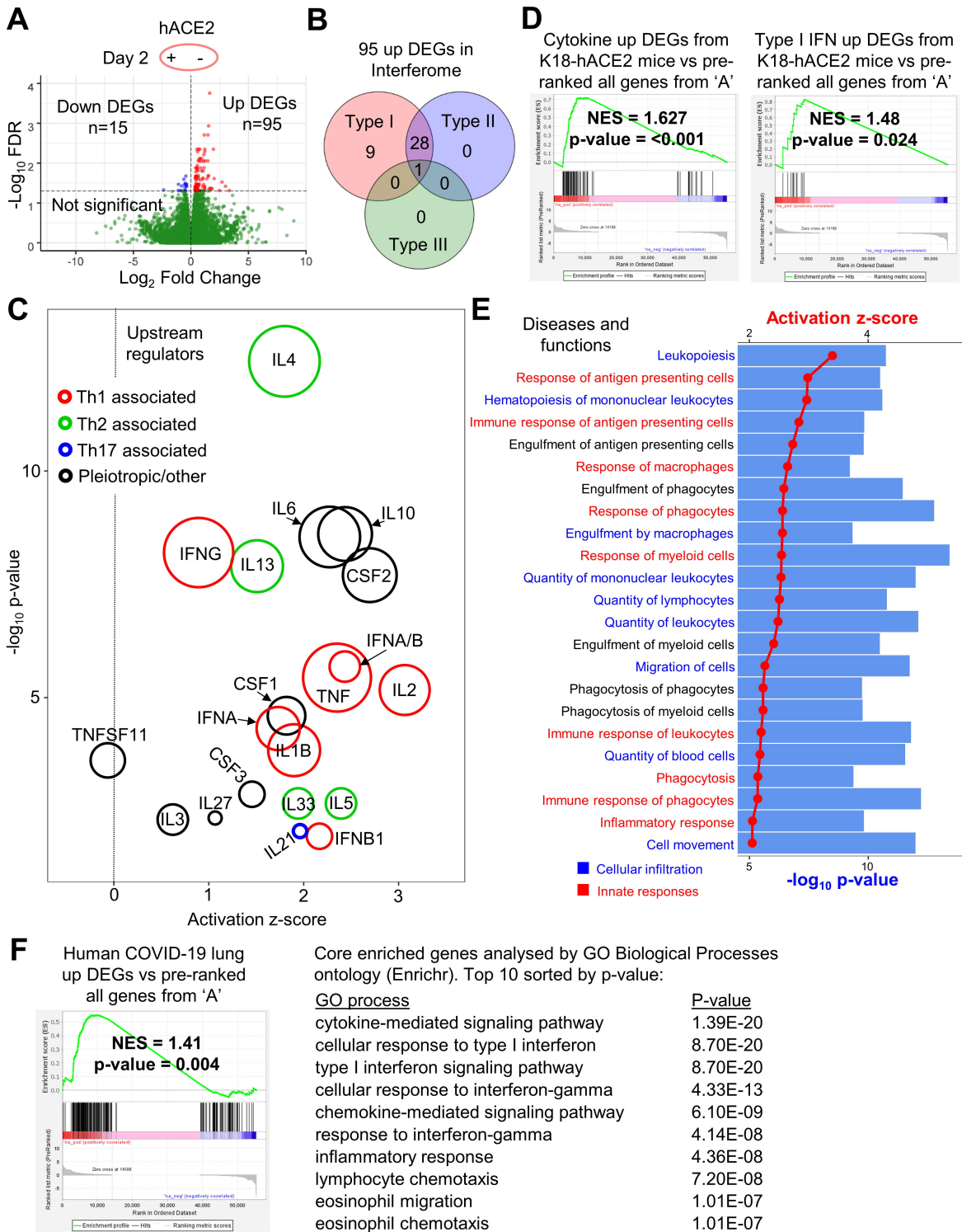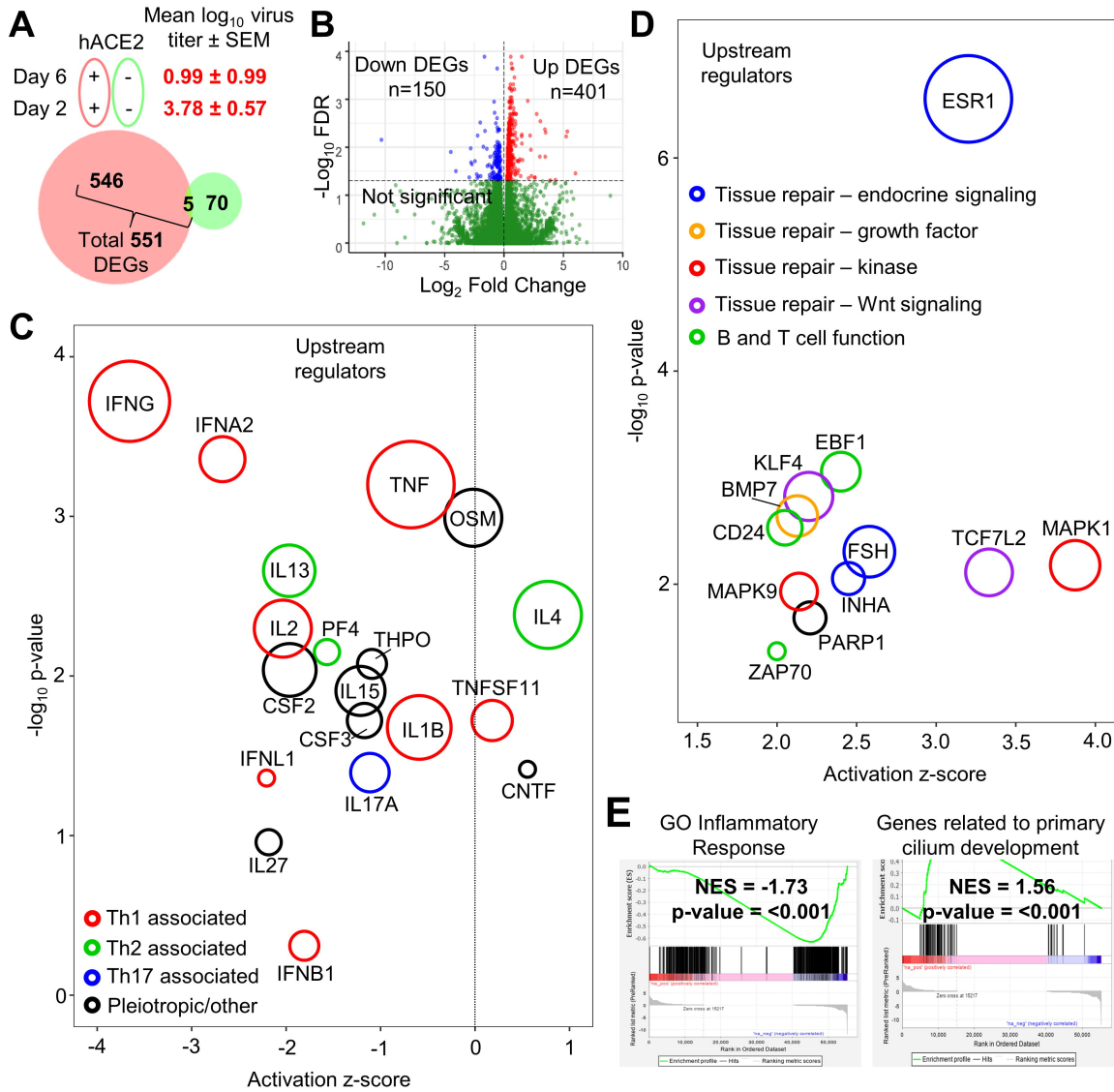
1123

# Figure 1

# Figure 2

# Figure 3



**A** hACE2 Day 2 (+ -)
Down DEGs n=15
Up DEGs n=95
Not significant
-Log₁₀ FDR / Log₂ Fold Change

**B** 95 up DEGs in Interferome
Type I: 9, 28, Type II: 0, 1, 0, 0, Type III: 0

**C** Upstream regulators
- Th1 associated (red)
- Th2 associated (green)
- Th17 associated (blue)
- Pleiotropic/other (black)
IL4, IL6, IL10, IFNG, IL13, CSF2, IFNA/B, CSF1, TNF, IL2, IFNA, IL1B, TNFSF11, CSF3, IL27, IL3, L33, IL5, IL21, IFNB1
-log₁₀ p-value / Activation z-score

**D** Cytokine up DEGs from K18-hACE2 mice vs pre-ranked all genes from 'A': NES = 1.627, p-value = <0.001
Type I IFN up DEGs from K18-hACE2 mice vs pre-ranked all genes from 'A': NES = 1.48, p-value = 0.024

**E** Diseases and functions — Activation z-score
- Leukopoiesis
- Response of antigen presenting cells
- Hematopoiesis of mononuclear leukocytes
- Immune response of antigen presenting cells
- Engulfment of antigen presenting cells
- Response of macrophages
- Engulfment of phagocytes
- Response of phagocytes
- Engulfment by macrophages
- Response of myeloid cells
- Quantity of mononuclear leukocytes
- Quantity of lymphocytes
- Quantity of leukocytes
- Engulfment of myeloid cells
- Migration of cells
- Phagocytosis of phagocytes
- Phagocytosis of myeloid cells
- Immune response of leukocytes
- Quantity of blood cells
- Phagocytosis
- Immune response of phagocytes
- Inflammatory response
- Cell movement
Cellular infiltration (blue), Innate responses (red)
-log₁₀ p-value

**F** Human COVID-19 lung up DEGs vs pre-ranked all genes from 'A': NES = 1.41, p-value = 0.004

Core enriched genes analysed by GO Biological Processes ontology (Enrichr). Top 10 sorted by p-value:

| GO process | P-value |
|---|---|
| cytokine-mediated signaling pathway | 1.39E-20 |
| cellular response to type I interferon | 8.70E-20 |
| type I interferon signaling pathway | 8.70E-20 |
| cellular response to interferon-gamma | 4.33E-13 |
| chemokine-mediated signaling pathway | 6.10E-09 |
| response to interferon-gamma | 4.14E-08 |
| inflammatory response | 4.36E-08 |
| lymphocyte chemotaxis | 7.20E-08 |
| eosinophil migration | 1.01E-07 |
| eosinophil chemotaxis | 1.01E-07 |

# Figure 4

# Figure 5

# Figure 6

**A**



**B** **C** **D**



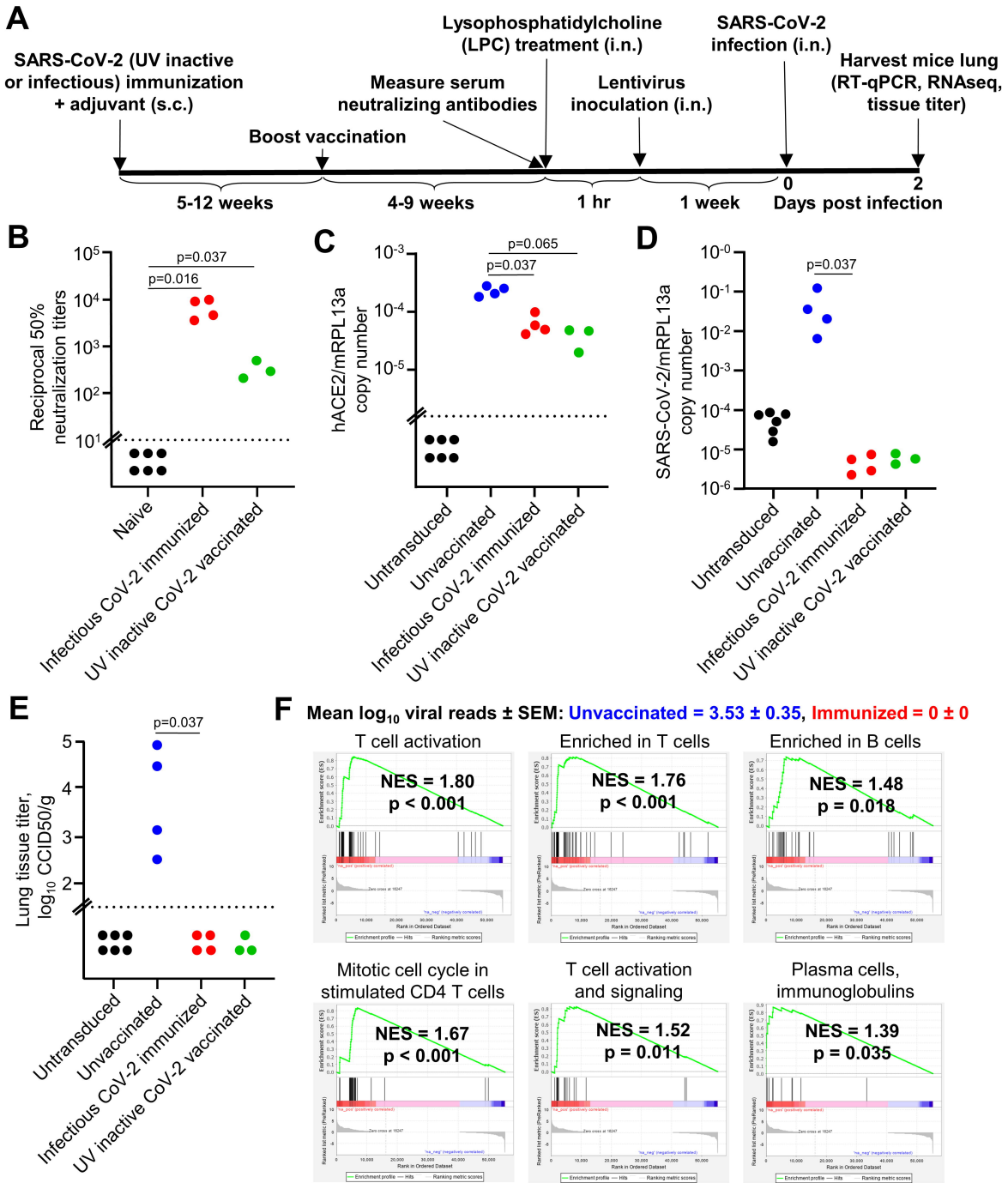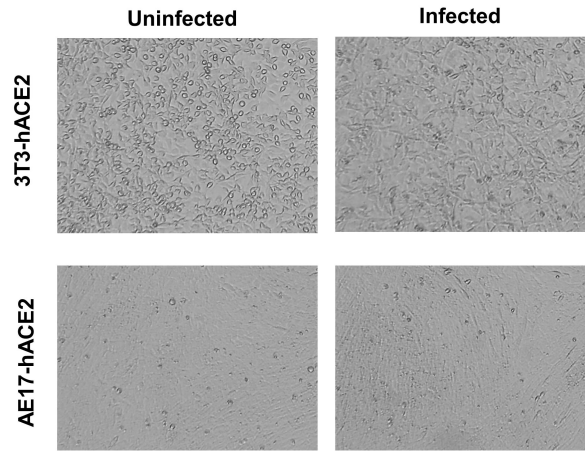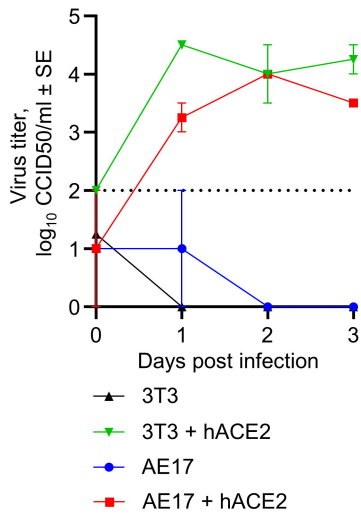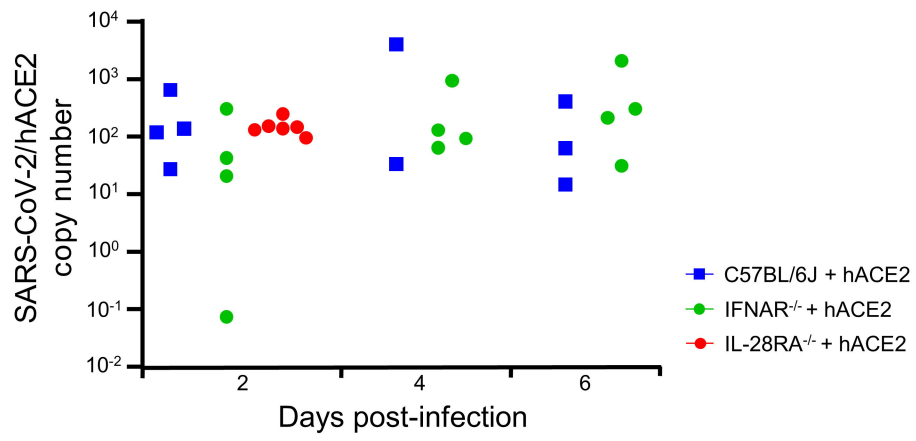**E** **F** Mean log$_{10}$ viral reads ± SEM: **Unvaccinated = 3.53 ± 0.35**, **Immunized = 0 ± 0**

# Supplementary figure 1

## Supplementary figure 2

# Supplementary figure 3



**Legend:** ● Untransduced C57BL/6J or IFNAR^{-/-}  ■ C57BL/6J + hACE2  ● IFNAR^{-/-} + hACE2  ● IL-28RA^{-/-} + hACE2

**A** — SARS-CoV-2/total read count vs Days post infection

**B** — hACE2/total read count vs Days post infection

**C** — SARS-CoV-2/hACE2 copy number vs Days post infection

**D** — orf1ab, S, E, M, N genome map (0 – 29,883); SARS-CoV-2 RNA reads